Design of a Rotary Reactor for Chemical-looping Combustion. Part 1: Fundamentals and Design Methodology

Zhenlong Zhao, Chukwunwike O. Iloeje, Tianjiao Chen, Ahmed F. Ghoniem[*]

Department of Mechanical Engineering, Massachusetts Institute of Technology

77 Massachusetts Avenue, Cambridge, MA 02139-4307, USA

Abstract

Chemical-looping combustion (CLC) is a novel and promising option for several applications including carbon capture (CC), fuel reforming, H_2 generation, etc. Previous studies demonstrated the feasibility of performing CLC in a novel rotary design with micro-channel structures. In the reactor, a solid wheel rotates between the fuel and air streams at the reactor inlet, and depleted air and product streams at exit. The rotary wheel consists of a large number of micro-channels with oxygen carriers (OC) coated on the inner surface of the channel walls. In the CC application, the OC oxidizes the fuel while the channel is in the fuel zone to generate undiluted CO_2, and is regenerated while the channel is in the air zone. In this two-part series, the effect of the reactor design parameters is evaluated and its performance with different oxygen carriers (OC) is compared. In Part 1, the design objectives and criteria are specified and the key parameters controlling the reactor performance are identified. The fundamental effect of the OC

[*] Corresponding author. Tel.: +1 617 253 2295.

E-mail address: ghoniem@mit.edu (A.F. Ghoniem)

characteristics, the design parameters, and the operating conditions are studied. The design procedures are presented on the basis of the relative importance of each parameter, enabling a systematic methodology of selecting the design parameters and the operating conditions with different OCs. Part 2 presents the application of the methodology to the designs with the three commonly used OCs, i.e., nickel, copper, and iron, and compares the simulated performances of the designs.

Keywords

Chemical-looping combustion; rotary reactor; CO_2 capture; oxygen carriers; reaction kinetics; reactor design

Content

Nomenclature

Symbols

A	cross-sectional area, m^2
C_i	concentration of species i, mol m^{-3}
C_f	friction coefficient

c	specific heat capacity, J kg^{-1} K^{-1}
D	reactor diameter, m
d_h	channel width, m
H	channel height, m
h_{gs}	heat transfer coefficient between phases, W m^{-2} K^{-1}
h_m	external mass transfer coefficient, m s^{-1}
Δh_r	enthalpy of reaction, J mol^{-1}
k	reaction rate constant
k_s, k_g	thermal conductivity of solid or gas phase, W m^{-1} K^{-1}
k_0	pre-exponential factor
m_ox	mass of fully oxidized oxygen carrier, kg
m_red	mass of fully reduced oxygen carrier, kg
$\dot{N}_f$	molar flow rate of fuel
P	operating pressure, Pa
P_c	inner perimeter of the channel, m
p_i	partial pressure of species i, Pa
R_oc	oxygen transport capacity
$\mathrm{R_u}$	gas universal constant, 8.314 J mol^{-1} K^{-1}
T	temperature, K
t	gas residence time in the channel, s^{-1}
u	velocity, m s^{-1}

$\dot{W}_{th}$	target thermal capacity, W
X	conversion of oxygen carrier
x_i	molar fraction of species *i*
$z_{99\%}$	height to reach 99% fuel conversion, m

Greek letters

δ_{bulk}	thickness of the bulk support layer, m
δ_{oc}	thickness of the porous oxygen carrier layer, m
ε	porosity of the OC
η_{I}	fuel conversion efficiency, percentage of fuel converted in the reactor
γ_{CH4}	conversion yield of CH_4
κ	redundancy factor
μ_g	viscosity of gas, kg m^{-1} s^{-1}
ν	stoichiometric coefficient
θ_i	size of sector *i*, rad
ρ	density, kg m^{-3}
τ	cycle period, characteristic time of reaction, channel residence time, s,
ω	rotational velocity, s^{-1}

Acronyms

CC	carbon capture

CCS	carbon capture and sequestration
CLC	chemical-looping combustion
OC	oxygen carrier
Redox	reduction and oxidation
TIT	turbine inlet temperature

1. Introduction

It has been widely accepted that fossil fuel combustion is a major contributor to the rise of CO_2 concentration in the atmosphere and global warming. One approach to reduce anthropogenic CO_2 emissions, apart from improving energy efficiency and using alternative sustainable energy sources, is carbon capture and sequestration (CCS), in which CO_2 is separated from flue gases, liquefied, and injected in geological formations, such as depleted oil or gas fields. Of these steps, CO_2 capture remains the most challenging part from an economic point of view since obtaining carbon dioxide in high purity still accounts for the major share of the cost of state-of-the-art CCS technologies. In the past few years, extensive research focus has been placed on three general processes for capturing CO_2 from combustion in power plants: post-combustion capture, pre-combustion decarbonization and oxy-combustion. One of the key issues that limits the applications of CCS approaches is the large energy penalty during the separation process.

Recently, a new approach for CO_2 capture has been widely investigated. This approach was named "chemical-looping combustion (CLC)"[1] and belongs to oxy-fuel combustion. In CLC, combustion is decomposed into two steps: fuel is oxidized by a metal oxide in a fuel reactor to generate CO_2 and steam; the reduced metal oxide is then regenerated by air in an air reactor. During this two-step process, the looping medium acts as an “oxygen carrier” (OC), which adsorbs oxygen in the air reactor and releases it to oxidize fuel in the fuel reactor. The main advantage of CLC is that by using OCs as the medium to transport the pure oxygen, the direct contact between air and fuel is circumvented and hence energy-intensive gas separation processes are avoided.

CLC is commonly carried out by physically transporting the oxygen carrier particles between two interconnected fluidized bed reactors [2-4]. In this reactor concept, the OCs in the form of particles are fluidized and pneumatically transported continuously between the fuel and air reactors. Several CLC units using the fluidized-bed design have been built and operated by Chalmers University of Technology of Sweden [5-8], ICB-CSIC of Spain [9-11], Vienna University of Technology of Austria [12, 13], and Southeast University of China [14, 15]. Meanwhile, some novel reactor designs have emerged such as the moving-bed reactor in Ohio State University [16, 17], the fixed packed-bed reactor in Eindhoven University of Technology of Netherlands [18, 19], and the rotating packed-bed reactor in SINTEF Materials & Chemistry of Norway [20, 21].

Recently, a rotary reactor design with micro-channel structures was proposed [22, 23]. As shown in Figure 1a, the reactor consists of a rotary wheel and two stationary chambers at the top and bottom of the wheel. The wheel rotates continuously through four sectors (Figure 1b): fuel, air, and two purging sectors. The rotary wheel consists of a large number of micro-channels (Figure 1c) with the OC coated onto their inner wall. As shown in Figure 1d, the channel wall has two solid layers with one being a highly porous OC layer and the other being a bulk dense ceramic layer with high thermal inertia and conductivity. The OC layer usually consists of an active metal oxide which reacts with the fuel and air alternatively, as well as an inert ceramic substrate which helps maintain the pore structures and chemical reactivities of the OC. As seen in Figure 2, pressurized feed gas (fuel, air or steam) flows through the reactor, reacts with the oxygen carrier (OC) while it is heated to high temperature. In the fuel sector, the fuel is diluted with CO_2 to effectively lower the operating temperature while in the air sector air is used to re-oxidize the OC. Two purging sectors are implemented between the fuel and the air sectors to sweep the residual gases out of the reactor. Flue streams from a large number of channels merge into two separate streams from the fuel zone and the air zone (see Figure 2b), respectively, and then drive turbines in the downstream, as described in ref. [22]. The main incentives for performing CLC in this way are (1) the separation of the gas and particles is intrinsically avoided, (2) the operation is continuous and stationary, and (3) the design is compact and easy to scale-up.

Pavone and co-workers [24, 25] simulated the reduction and oxidation (redox) performances of the rotary reactor with nickel oxide wash-coated on alumina substrate using COMSOL for the initial cycles. Because of the limited amount of the solid phase in the base-case design, large temperature fluctuations (500℃) were observed in the solid phase, which renders the design unstable over repeated cycles. Zhao et al. [26] investigated the periodic stationary-state performances of a rotary design with copper oxide supported on boron nitride substrate using a one-dimensional plug-flow model. The base-case simulation validated the applicability of the rotary design to the CLC process with high separation efficiency and operational stability. However, the sensitivity study showed that the performances are highly dependent on the selection of OCs, the designs of the reactor, and the operating conditions. These parameters are highly coupled, and they are all closely related to the performances of the reactor. Therefore, the fundamentals of such a system and effects of design parameters must be studied thoroughly and systematic approaches and methodologies of selecting the design and operating conditions should be investigated in depth.

The aim of this two-part series is to investigate the fundamental effects of design on the rotary reactor performances, and to propose a comprehensive methodology of selecting the suitable materials and the operating conditions. In Part 1, the design objectives and criteria are discussed. The fundamental effects of the OC characteristics, the design parameters, and the operating conditions are studied. The design procedures are presented on the basis of the relative importance of each parameter, enabling a systematic methodology of selecting the design parameters and the operating conditions with different OCs. Part 2 presents the application of the methodology to the designs with the three commonly used OCs, i.e., nickel, copper, and iron, and compares the simulated performances of the designs.

2. Design Objectives and Criteria

The design of the rotary CLC reactor should satisfy a number of requirements, including (1) complete fuel conversion, (2) CO_2 separation, and (3) operational stabilities during repeated cycles. In addition, the reactor design should also be (4) compatible and easy to integrate with the power cycle, and (5) economically feasible with low fabrication cost. This section addresses the objectives and the criteria of design and also identifies the key parameters that control the reactor performance.

2.1 Fuel Conversion

High fuel conversion is required for the reactor design. Fuel conversion is controlled by the reduction reaction between the gaseous fuel and the active metal oxide on the surface. For this purpose, one needs to (1) use an OC layer with highly reactive metal oxides, (2) operate at favorable conditions (T_{in}, P, etc.), or (3) provide sufficient residence time (t_{fuel}) of gas.

As seen in Figure 3, the reduction reaction within the reactor generally involves several key steps: external and internal diffusions, adsorption and dissociation, diffusion through the grain, and reactions. Table 1 summarizes the characteristic times for the conversion of the OC under each resistance (see Section 3.1.1 for derivation). A highly reactive metal oxide, e.g., nickel-, copper-oxide, with a suitable oxidation state, e.g., Fe_2O_3/Fe_3O_4, favors the conversion efficiency. In addition, properly selected OC preparation methods and layer designs minimize the resistance from each intermediate step. For instance, as seen in Table 1, smaller channels with a higher convective transport rate (h_{m}) reduces the external resistance; a higher porosity increases the effective diffusivity (D_e) through the pores and thus enhances internal diffusion; a highly porous OC layer with large specific areas (s_{oc}) decreases the resistances from steps 3-5 (Table 1) by providing a larger number of active sites and enhancing the contact between the gas and solid phases; thin grain layers (δ_{grain}) with well-dispersed active metal oxides on the support effectively reduce the product layer diffusion resistance through the grain and thus enhance the exposure of the embedded ions to the gaseous reactants. For an optimized design, the rule of thumb is to minimize the resistance from each step and maintain $\mathrm{Da_i}$ below 0.1. As a result, the reaction should be mainly controlled by the intrinsic chemical kinetics of the selected metal oxide.

To further raise the fuel conversion rate, favorable operating conditions can be selected on the basis of the OCs. Higher fuel concentration or temperature always accelerates the reaction rate, although the dependency varies significantly among different OCs. For example, as noted in Part 2, the reduction rate of the iron-based OC is mostly sensitive to the concentration of the fuel while the high endothermicity of nickel oxide reduction leads to a high reaction barrier and therefore the rate correlates with the temperature. Operating pressures (*P*) may also affect the reaction rate because the gas composition, the species diffusion, the fuel adsorption, the morphology and topology of the grain, and the amount of the active sites on the grain may change with pressure. The degree of OC conversion also has influences on the reduction rate, and generally the reaction rate is highest initially, and slows down as the conversion proceeds. Thus, an intermediate OC conversion is usually preferred, where the OC is neither fully oxidized nor fully reduced [17].

Adequate residence time of the gas in the channel (t_{fuel}) should be maintained to ensure complete fuel consumption:

$$t_{fuel} = \int_0^H \frac{dz}{u_{fuel}} \geq t_{99\%,\,fuel} \quad (1)$$

Here, $t_{99\%,fuel}$ is the characteristic time of 99% fuel conversion, u_{fuel} is the bulk velocity in the fuel sector, and H is the height of the reactor channels. To increase the residence time (t_{fuel}), one can use longer channels (H) or a lower velocity (u_{fuel}), both of which, however, require a larger reactor to reach the target thermal output, and hence increase the fabrication cost. On the other hand, the characteristic time ($t_{99\%,fuel}$) for conversion can be reduced by admitting the same amount fuel at the inlet with a lower flow rate but a higher concentration (x_{fuel}). Thus, the high fuel concentration favors the reactivity and hence enhances the conversion (see Part 2). However, this effect may be weakened when most of the OC near the inlet is consumed by fuel, leading to a decreased reaction rate near the inlet and thus an gradually increased $t_{99\%,fuel}$. Besides, a higher air flow rate (u_{air}) is usually required to effectively transfer the reaction heat by convection, since in this case less dilute gas (CO_2) is fed in the fuel sector.

2.2 Carbon Separation

To capture CO_2 generated in the fuel sector, the residual gas inside the channel should be purged within the fuel purge sector. Similarly, the residual air inside the channel should be removed as the channel passes through the air purge sector. Thus, the design requires that

$$t_i = \int_0^H \frac{dz}{u_i} \le \tau_i = \frac{\theta_i}{\omega} \quad i = \text{fuel purge or air purge} \quad (2)$$

t_i being the residence time of gas, u_i the purge velocity, τ_{i} the residence time of the channel in the (fuel or air) purge sector, θ_i the purge sector size and ω the rotational velocity. To reduce t_i, shorter channels (H) and higher purge velocities (u_i) are preferred in both purge sectors. However, a sufficient $t_{fuel\ purge}$ should be adapted, i.e., $t_{\mathrm{fuel,\ purge}} \ge t_{99\%,\ \mathrm{fuel\ purge}}$, to convert the residual fuel within the channel, similar as in the fuel sector (Eq. (1)). In contrast, the steam velocity in the air purge sector can be much higher and hence $t_{air,\ purge}$ can be greatly decreased. Thus, the fuel purge sector generally takes a larger share of the reactor than the air purge sector. On the other hand, one can improve the separation efficiency by using a slower rotational velocity (ω). A slower rotational velocity (ω) increases the residence time of each channel in the purging sector (τ_i). Therefore, more purging steam flushes through the reactor to clean up the residual gas (CO_2, or O_2/N_2). The decrease of ω, however, is constrained by the concerns of fuel conversion and the thermal stability of the reactor [26, 27]: (1) at a slower ω, and consequently a longer residence time of channel within the fuel sector (τ_{fuel}), more OCs are consumed by fuel, leading to a reduced reduction rate, and hence potentially a lower fuel conversion efficiency; (2) more chemical energy is released from the redox reactions during one cycle, leading to a larger temperature fluctuation.

In addition, the fuel leakage and the air dilution between the fuel and air zones will decrease the separation efficiency. In the rotary reactor, gas leakage may originate from the pressure difference between adjacent sectors, as well as the spinning motion of the rotary wheel [22]. To minimize the pressure-driven gas leakage, relatively uniform operating pressure (P) is recommended in the system among different sectors. In addition, the pressure drop along the channel caused by skin friction should be similar among different channels in order to match the pressure distribution in both feed and exit chambers. Therefore, the similar feed velocities are recommended among different sectors, while steady conversion patterns are preferred to minimize the pressure field variation within the reactor. Effective sealing systems (brush seals, labyrinth seals [28]) from gas turbines can be readily adapted to the rotary reactor to avoid the spinning-driven dilution between the fuel and the air zones.

Carbon deposition on the channel walls during the fuel sector may be transported to the following air sector, leading to reduced separation efficiency. The deposition of carbon mainly depends on the type of the material and the availability of oxygen [4]. Metal catalysts may catalyze the fuel decomposition reaction, and lead to the formation of carbon. This appears more prominent near the end of the reduction period as the majority of the OC is consumed [29]. On the other hand, deposited carbon can be eliminated via gasification with H_2O or CO_2 [30-34] or the solid-solid reaction between carbon and the lattice oxygen in the OC [35]. Therefore, there is usually a balance between carbon formation and disappearance, and thermodynamic equilibrium usually determines the relative importance of them. Adding sufficient H_2O (or CO_2) [36] and maintaining sufficient oxygen within the OC [22] shift the equilibrium and hence mitigate the carbon formation risk.

2.3 Operational Stability

The most important aspects of the operational stability are that (1) the OC be chemically stable and consistent as it is repeatedly exposed to the reducing and oxidizing environments; (2) the two-layer structure be thermally stable and resistant to thermal stresses associated with temperature variations; and (3) the performances of the reactor be robust to the uncertainties with the operations.

Extensive experiments on nickel-, copper-, and iron-based metal oxides have illustrated their long-term repeatability as OCs for CLC, while manganese-, cobalt-, or calcium sulfate-based OCs may decompose under high temperature or with the presence of CO_2 and steam in the reactor [4]. The inert substrate in the porous layer should act as a structure support to improve the gas permeability, enhance the active surface areas, sustain the stresses during cyclic operations, and hence improve the chemical stability of the OCs. Ceramics (e.g., Al_2O_3, YSZ) are commonly suggested as the proper binder materials because of their excellent corrosion resistance under high-temperature oxidizing environment. The support material should also be compatible to the selected metal oxide.

In addition, the OC should be sufficiently resistant to carbon deposition, melting and agglomeration, and impurity species (e.g., sulfur) in the feed gas. As discussed before, carbon formation risk can be mitigated by selecting less catalyzing materials, adding CO_2 and/or steam, or maintaining sufficient oxygen within the OCs during the fuel sector. The melting of the materials (e.g., metal oxide, support substrate, or impurities) within the porous layer may lead to irreversible changes of the pore structure. The impurities, such as H_2S, within the gaseous fuel may react with the active metal oxide to form compounds that are poisonous to the OCs, decrease the OC capacity, block the pore structure, and significantly impairs the stability, and thus it is generally preferred to operate under an impurity-free environment [4].

The thermal stability requires the reactor be resistant to the thermal stresses during the repeated cycles. The thermal expansions induced instabilities in the reactor primarily originate from the mismatch of the support materials in the two-layer structure, the axial temperature variation, and the peripheral temperature fluctuation:

- Similar support materials with high toughness but low coefficient of thermal expansion should be used to match the expansion of the porous and the dense layers, and hence reduce the thermal distortion and stresses between the two layers;
- In the periodic operation, the solid temperature increases from the inlet to the exit. The axial temperature variations are accompanied by differential thermal expansion. Thus, sufficient

clearances should be maintained between the rotary wheel and the outer insulating walls to account for the expansion. To minimize the differential expansion along the channel, a thick and highly conductive dense support layer is preferred to effectively transfer the heat from the exit to the inlet.

- The local solid temperature may vary with time as the channel moves through different sectors due to the mismatch between the reaction heat release, conduction and convective cooling [26]. Localized hotspots can lead to thermal-stress-induced fracture among the channels at the same axial location but different angles in the wheel. Thick dense layers with high thermal inertia mitigate the peripheral thermal stresses by providing a large heat reservoir to match the difference and thus minimize the fluctuation. A faster spinning velocity and hence a shorter cycle period also reduce the fluctuations.

The design of the reactor should possess sufficient operational safety margins to deal with uncertainties from the start-up of the operation, and off-design deviation during continuous operation. The start-up period of the rotary reactor may take hours, or even a few days because of the large thermal inertia of the solid wheel and the non-uniform temperature distribution along the axis of the reactor under periodic stationary states. Adequate redundancy should be applied to the rotary wheel and the ancillary parts (e.g., insulating walls, bearing) to stand the temperatures and the pressures during the start-up period. In periodic stationary state, the performances of the reactor should be robust under minor deviation of the operating conditions from the set point. A sufficient redundant length (e.g., 25% of the reactor height), should be adopted near the exit of the reactor to ensure fuel conversion and avoid extinction of combustion. Real-time monitor of the performances (temperature, flue species) and active controls of the feed flows should also be applied to effectively maintain the stability.

2.4 System Integration

The integration with the power generation system is the ultimate goal of the design of the rotary CLC reactor. To maximize the system efficiency, it is critical to minimize the exergy loss. Studies showed that for power generation systems with CLC, the largest irreversibility occurs in the reactor [1]. To reduce this loss, it is preferred to operate the redox reactions isothermally at temperatures close to equilibrium.

For CLC reactors, the operating temperature is constrained by the material. For the OCs with low melting point (e.g., 1085℃ for copper), supplemental firing may be required to further raise the flue stream temperature to improve the system efficiency, which decreases the CO_2 separation efficiency. The maximum allowable turbine inlet temperature (TIT) places an upper limit on the reactor exit temperature, and supplemental cooling is required if the flue gas temperature is beyond the material limit of the gas turbine.

Isothermal operations in the fuel and air sectors are advantageous in enhancing the reaction rates, and eliminating the entropy generation associated with the heat transfer within the reactor. Thermodynamic analysis shows that for the CLC with endothermic reduction, higher work output may be achieved, by operating the reduction at a lower temperature and utilizing a secondary engine to extract work while transferring the heat from the air to the fuel sector. From a practical point of view, however, the installation of such engine is less feasible, and hence it is preferred to operate the redox reactions at the same temperatures (see Appendix A).

To reach isothermal operation in the reactor, it is critical to utilize a thick dense layer with high thermal inertia and conductivity, that temporally stores energy from the exothermic reaction, and distribute it throughout the reactor. Preheating the feed streams in the power generation system improves the isothermality by reducing the temperature difference between the gas and the solid near the inlet of the reactor. This can be achieved in a simple Brayton cycle with effective exhaust recuperation. The design choice depends on the exergy cost of non-isothermal reactor operation, the preheating options in the system, as well as the cost implications.

The selection of the operating pressure in a CLC system generally depends on the power cycle. Generally, the efficiency of the system increases with the compressor pressure ratio until it reaches an optimal value, which depends on the balance between work extracted from the turbine and the corresponding energy consumed in the compressor. It has been shown, at least for a combined cycle CLC system, to be tied to the selected TIT [37, 38]. Additionally, the operating pressure may also affect the reactivity of OCs, as discussed in Section 2.1.

2.5 Costs of Fabrication

The costs of fabrication are determined mainly by the size of the reactor, the raw material of the OCs and the substrate, and the fabrication techniques. The reactor size is determined by the diameter, which is chosen to reach the target thermal capacity; and the height, which is selected to ensure fuel conversion. For raw OC materials, promising candidates are oxides of copper, nickel, cobalt, iron and manganese, because of their high fuel conversion and oxygen transport capabilities, among which copper, manganese and iron are cheaper than nickel and cobalt. As for cost of the support material, alumina is among the cheapest and is easier to manufacture. However, materials like boron nitride, beryllium oxide, aluminum nitride, and silicon carbide are still the favorable choice in spite of the high cost because of their higher thermal conductivity, which is crucial to the thermal stability of the reactor.

The fabrication may follow the industrial experiences of microchannel reactors, such as the catalytic converter, the microchannel heat exchanger [39], the microchannel Fischer-Tropsch reactor [40], etc. For example, one approach to manufacture the structural channels of the rotary wheel is the conventional powder compaction technique. The selected ceramic powder, such as alumina, mixed with appropriate binder, is spray-dried with custom dies to form the channel geometries. It is then laminated by high-pressure hydraulic presses, and sintered at high temperature. The active OC can then be wash-coated onto the inner walls of the ceramic reactor and then calcined at high temperature to form the porous OC layer.

3. Design Fundamentals

To achieve the design objectives listed in Section 2, a variety of parameters can be selected. The design parameters can be grouped into three categories [22]: (1) material selection; (2) reactor design; (3) operating conditions. All of these parameters are highly coupled, as illustrated in Section 2, and they all strongly affect the performances of the reactor. Thus, it is critical to understand the fundamentals of the design, the relative importance of each parameter, and the underlying logics to choose the optimal values of all the variables.

3.1 Material Selection

3.1.1 Porous OC layer

The quality of the OC is the most important aspect for the viability of CLC. A suitable OC should possess the following characteristics [3, 4]: (1) high reactivity; (2) reasonable stability; (3) abundant in nature and feasible for large-scale operations. Different metal oxides have been proposed, among which, nickel [35, 41-44], copper [41, 44-48], and iron [41, 49-51] are the most promising OC candidates. Table 2 summarizes the key properties and the redox reactions of these OCs. The reaction heat affects the heat balance in one cycle. A highly exothermic oxidation in the air sector usually leads to a rapid rise of the reactor temperature while an endothermic reduction extracts heat from the solid phase to sustain the reactivity. Flow streams further absorb heat from the reactor via convective heat transfer. Thus for nickel or iron, localized hot-spots (or cold-spots) are expected in the air (or fuel) sector while for copper, the temperature fluctuation can be minimized by matching the redox heat release and heat convection in both fuel and air sectors. The equilibrium conversion yield of the OC indicates the maximum conversion of fuels. For CH_4, the conversion yield is defined as $\gamma_{CH4} = p_{CO2} / (p_{CO2} + p_{CO} + p_{CH4})$, where p_i are the partial pressures of species i. All the three OCs have close to unity equilibrium conversion yields, although the yield for nickel slightly decreases at 1200℃ owing to the presence of CO in equilibrium.

The oxygen transport capacity, defined as $R_{oc} = (m_{ox} - m_{red})/m_{ox}$, where m_{ox} and m_{red} are the masses of the fully oxidized and reduced OC, respectively, describes the maximum amount of oxygen that can be carried by the OC between the fuel and air sector. The oxygen transport capacity decreases as inert binders are added in the OC. R_{oc} is usually related to the cycle period, τ, and the circulation rate of the porous OC, $\dot{m}_{OC}$, as:

$$\dot{m}_{OC} = \frac{N \rho_{oc} A_{oc} H}{\tau} = \frac{v M_O \dot{N}_f}{R_{oc} \Delta X_{oc}} \quad (3)$$

N being the total number of channel in the wheel, δ_{oc} the total thickness of the OC layer within each channel, ρ_{oc} and A_{oc} the density and the cross-sectional area of the OC layer, H the height of the reactor. M_O is the atomic weight of oxygen, $\dot{N}_f$ is the molar flow rate of fuel admitted in to reactor, and v is the stoichiometric coefficient. ΔX_{oc} is the difference in the OC conversion between the fuel and air zones. Copper and nickel have similar oxygen transport capacity, while iron has a relatively lower capacity. Thus a larger OC circulation rate is needed for the iron-based design to reach the same thermal capacity. From Eq. (3) it is also obvious that for a design with a thicker OC layer and faster rotational velocity, more fuel can be admitted into the reactor, and hence, a smaller reactor is needed to reach a certain capacity.

The melting point of the metal oxides is an important parameter in determining the operating temperature. Because of its the low melting temperature, copper as OC particles is usually operated under 1000℃ [4, 9, 10, 52-54]. In addition, due to the low melting point, dry (or wet) impregnation method is commonly used to prepare the copper-based OCs [4], which produces a highly porous and uniform structure to provide competitive reactivities at lower temperature and maintain stability during repeated cycles. However, the low loading content in the OC, resulting from the preparation method, leads to a reduced oxygen transport capacity, R_{oc}.

Carbon deposition reduces the separation efficiency, deactivates the surface catalytic reactions by blocking the active surface areas, and leads to operational failure, as discussed in Section 2. Experiments [34, 35, 42, 43, 55, 56] showed that metallic nickel, known as catalyst to pyrolysis and Boudouard reactions, favors methane cracking and thus increases the tendency of carbon formation. On the contrary, no or very limited carbon formation has been observed for copper- and iron-based under the operating conditions of interests [29, 57]. In addition, carbon formation is strongly dependent on the amount of oxygen available, either from the OC [22, 35, 36] or from steam [31, 34], and becomes more prominent at the end of the reduction period when the majority of the available oxygen is consumed [29, 57]. Thus, sufficient oxygen should be maintained within the OC layers during continuous operation, especially for the nickel-based design, and adequate purging steam is necessary to effectively clean up deposited carbon.

The porous OC layer also consists of inert materials which act as a structural support maintaining the pore structures, improving the gas permeability, providing a higher active surface area for reaction, and increasing the mechanical strength of the layer. The inert materials in the OC layer should possess sufficiently resistance to thermal stresses and remain nonreactive under the redox environment. In addition, the inert material should also be sufficient bonding yet unreactive with the active metal oxide. Potential options for the rotary design may include (but not limited to) BN, AlN, BeO, SiC, Al_2O_3, Si_3N_4, ZrO_2, TiO_2, YSZ.

3.1.1.1 Reactivity

The redox reactivity is one of the most important properties of the OC, as it directly determines the fuel conversion. Generally, the overall redox reactions are represented by

A (g) + ν_r B (s) $\rightarrow \nu$ C (s) + D (g) (4)

where A represents fuel for reduction, and O_2 for oxidation. B is the active metal oxide (or metal) within the porous layer, and ν_r is the stoichiometric coefficient. As described in Section 2, the conversion may invlove several key intermediate steps [4, 58, 59]: (1) the external diffusion of the reactants from the bulk of the gas phase to the surface of the OCs (Figure 4a); (2) the internal diffusion of gaseous reactants through the pores of the OCs to each active grain of the metal oxide (Figure 4b); (3) the adsorption of the gaseous reactants onto the active metal oxide lattice surface (Figure 5); (4) the diffusion of the reactants through the grain layer (Figure 6); (5) the intrinsic chemical reaction of the reactants. Gaseous compounds produced during the reaction go through desorption and diffusion via the opposite direction from steps (3) – (1).

The following discussion in this section applies simple models to evaluate the conversion process in which steps (1) – (5), in turn, are rate-controlling, with a focus on a plat-like porous OC geometry resembling the layout of the micro-channel design. The characteristic time of conversion for each resistance is derived and listed in Table 1. The Damköhler numbers (Da) for the intermediate resistances (steps 1-4) can be calculated as the ratio of the characteristic time of that step to that of the chemical reaction (step 5), and it provides an effective approach to identify the key parameters that ultimately determine the overall reaction rates for a specific OC. Part 2 of this series follows this method to select the design parameters and operating conditions suitable for three different OCs of CLC.

To account for the simultaneous action of these steps, one can combine these resistances in series with their individual driving forces and fluxes, following the electrical circuit analogy, and develop a detailed model to capture the spatial and temporal resolutions of this process. This will be addressed in depth in the future.

Chemical Kinetics Control

The intrinsic rate of reaction under the control of the chemical kinetics can be expressed as (see Appendix B for derivation):

$$-\frac{1}{\nu_r}\frac{dN_B}{dt} = -\frac{dN_A}{dt} = k_r N_s C_A \phi_B \quad (5)$$

where k_r is the reaction rate coefficient, N_B is the total moles of B. Here, a first-order irreversible reaction is assumed. For an OC layer with outer surface area of S_o, thickness of δ_{oc}, and an initial molar density of $\hat{\rho}_B$ (moles/m^3 OC layer), the amount of metal oxide present in the OC layer is $N_B = \left(1 - X_B\right)\hat{\rho}_B S_o \delta_{oc}$, where X_B is the conversion of reaction. N_s is the total number of the active sites, calculated as $N_s = \tilde{\rho}_s s_{oc}\delta_{oc}S_o$, with $\tilde{\rho}_s$ being the concentration of the active site on the surface and s_{oc} the specific surface area per unit volume (m^2 grain/m^3 OC layer) of the active grains. ϕ_B is the coverage of solid reactant B in the lattice grain, and equals $1 - X_B$. Thus, we can integrate Eq.(5) to obtain the logarithmic rate law as:

$$-\ln\left(1 - X_B\right) = t/\tau_r,\ \tau_r = \frac{\hat{\rho}_B}{\nu_r s_{oc}\tilde{\rho}_s k_r C_A} \quad (6)$$

From Eq.(5), a thicker OC layer (δ_{oc}) and hence a larger amount of metal oxide are recommended to improve the fuel consumption rate (-dN_A/dt). As seen in Eq. (6), a higher specific surface area of the OC (s_{oc}) and a more uniform dispersion of the metal oxide on the porous substrate ($\tilde{\rho}_s$) should be used to reach a fast reaction rate between the solid and the gas.

External Diffusion Controls

As shown in panel a of Figure 4, if the process is controlled by external diffusion, the concentration of reactant *A* drops from its bulk value to zero within the gas film adjacent to the outer surface of the porous OC layer. In this case, the rate of OC conversion can be expressed as:

$$-\frac{1}{\nu_r}\frac{dN_B}{dt} = S_o h_m C_A \quad (7)$$

C_A being the concentrations of reactant *A* in the bulk, and h_m the mass transfer coefficient. N_B is the total moles of the metal oxide (or metal). Thus we can obtain the linear rate law of conversion as:

$$X_B = t/\tau_{ex},\ \tau_{ex} = \frac{\hat{\rho}_B \delta_{oc}}{\nu_r h_m C_A} \quad (8)$$

For a fully developed laminar channel flow, the convective mass transfer coefficient, h_m, can be calculated as, $h_m = Sh_d \cdot D_M / d_h$, where Sh_d is the Sherwood number, and d_h is the hydraulic diameter. The Sherwood number depends on the geometry of the channel. D_M is the molecular diffusivity of reactant in the bulk flow, which can be determined using Fuller's correlation [60]:

$$D_M = \frac{10^{-3} T^{1.75} \left(M_A^{-1} + M_i^{-1}\right)^{0.5}}{P\left[\left(\Sigma_v\right)_A^{1/3} + \left(\Sigma_v\right)_i^{1/3}\right]^2} \quad (9)$$

where *T* and *P* are the temperature and the pressure. M and Σ_v are the molar mass and the diffusion volume, respectively. The Damköhler number for the external diffusion is:

$$Da_{ex} = \frac{s_{oc} \tilde{\rho}_s k_r \delta_{oc}}{h_m} \quad (10)$$

Eq (10) shows that to reduce the resistance of the external mass diffusion, a small channel with a thin OC layer are recommended. In addition, a higher operating temperature with a low pressure also favors the diffusivitiy and hence further decreases Da_{ex}.

Internal Diffusion Controls

Figure 4b shows the OC covnersion process in which the internal diffusion through the pores controls the reaction rate. In this case, because of the fast external diffusion, the concentration of *A* at the exterior surface is the same as that in the bulk flow. Thus, a slowly shrinking unreacted core is expected, inside which the solid reactant *B* remains unreacted, as illustrated in Figure 4b. The reaction occurs only on the boundary of the unreacted core, shrinks the core size, and leaves behind a gradually thickening diffusion layer. Thus, the rate of conversion can be expressed on the basis of the unreacted shrinking-core model (USCM) as:

$$-\frac{1}{\nu_r}\frac{dN_B}{dt} = S_o D_e \frac{C_A}{\left(\delta_{oc} - z_{un}\right)} \quad (11)$$

D_e being the effective diffusivitiy, and z_{un} the thickness of unreacted core. By integrating Eq. (11), we can obtain the parabolic law of conversion as:

$$X_B^2 = t / \tau_{in}, \quad \tau_{in} = \frac{\hat{\rho}_B \delta_{oc}^2}{2\nu_r C_A D_e} \quad (12)$$

The effective diffusivity, D_e, can be evaluated as a combination of the molecular and Knudsen diffusions as [61]:

$$D_e = \varepsilon^2 / \left[\frac{1}{D_K} + \frac{1}{D_M}\right] \quad (13)$$

where ε is the porosity of the OC layer. The Knudsen diffusivity, D_K, can be determined as [62]:

$$D_K = \frac{8\varepsilon}{3s_{oc}}\sqrt{\frac{2R_uT}{\pi M_A}} \quad (14)$$

The Damköhler number for the external diffusion can then be expressed as:

$$Da_{in} = \frac{s_{oc}\tilde{\rho}_s k_r \delta_{oc}^2}{2D_e} \quad (15)$$

From Eq. (15), it is clear that a thin OC layer significantly reduces the internal mass diffusion resistance. In addition, a higher porosity of the OC layer increases the effective diffusivity through the pores and hence favors the internal diffusion.

Adsorption Process Controls

As the reactant approaches the grain surface, gaseous molecules adsorb onto the lattice crystals and dissociate while catalyze by the metal ion on the surface. In the reduction process, the dissociated protons from the fuel bond to the oxygen ions on the lattice surface, forming substitutional hydroxyl defects [63], as seen in Figure 5a. The dissociated molecules may further migrate within the lattice, break metal oxide bonds, and consume the lattice oxygen ions. The metal cations may migrate within the grain, collapse into clusters, grow, and finally overlap to form crystallites of the solid product [58]. During the oxidation, the oxygen molecules are ionized by the electrons within the lattice, occupying active sites and forming electron holes [64], as seen in Figure 5b. The dissociated oxygen atom may dissolve within the grain while the metal cations may migrate to partner the adsorbed oxygen on the grain surface [65]. These processes are complicated, and involve several intermediate steps [58, 59, 66]. Here, the Eley-Rideal reaction mechanism is used to qualitatively model the adsorption process, as follows:

A (g) + S (s) $\leftrightarrow$ AS (s) (16)

AS (s) + ν_r B (s) $\rightarrow$ ν_p C (s) + D (g) (17)

where AS represents the adsorbed molecule on the lattice, and S is the open site in the lattice. Assuming that the adsorption reaction (16) controls the conversion, we can obtain (see Appendix B for derivation):

$$-\frac{1}{\nu_r}\frac{dN_B}{dt} = k_{ad} N_s C_A \quad (18)$$

where k_{ad} are the reaction rate coefficient of the forward reaction (16). By integrating Eq.(18), we can obtain the linear law of conversion as:

$$X_B = t / \tau_{ad}\,,\ \tau_{ad} = \frac{\hat{\rho}_B}{\nu_r s_{oc} \tilde{\rho}_s k_{ad} C_A} \quad (19)$$

The Damköhler number for the adsorption process can thus be expressed as:

$$Da_{ad} = \frac{k_r}{k_{ad}} \quad (20)$$

As conversion proceeds, however, the available active sites, N_s changes. In addition, the nature of the sites, S, also greatly influences the adsorption rate. As an example, an induction period of NiO reduction process has been clearly observed, during which NiO slowly adsorbs fuel molecules and reacts to form metallic nickel nuclei. As nuclei grows, an autocatalytic reduction period occurs where the fuel is rapidly dissociated by the metallic Ni clusters [67, 68]. Thus, during this two-stage conversion process, the active site in the lattice alters significantly. As reduction proceeds, the metallic nuclei agglomerate to form clusters, leading to the decrease of the available sites on the lattice surface. Besides, the diluent molecules (e.g., H_2O, CO_2, N_2) may adsorb onto the catalytic medium, occupy the open sites and hence inhibit the adsorption process

[58, 69]. As a result, the conversion process controlled by adsorption usually shows a sigmoidal conversion-versus-time profile, as documented in the literature [4, 58, 64]. The conversion rate is slow initially because of the lack of catalytic nuclei, and also near the completion with few available ions present on the surface and product molecules occupying the available sites. To account for these effects, the number of the active sites can be modeled using the Avrami-Erofeev Model (AEM) [4], as:

$$N_s = N_{s,0}\beta\left(1-X_B\right)\left[-\ln\left(1-X_B\right)\right]^{(\beta-1)/\beta} \quad (21)$$

where β is the Avrami exponent indicative of the adsorption mechanisms. The term, $\beta[-\ln(1-X_B)]^{(\beta-1)/\beta}$ represents dynamic changes of the active sites.

Grain Diffusion Controls

As seen in Figure 6, it is clear that the solid reaction product (metal for reduction and metal oxidation for oxidation) separates the two reactants (A and B). In order for the reaction to further proceed, one or both reactants must penetrate the product layer: the dissociated ions (e.g. H^+, O^{2-}) on the grain surface may transport into the grain lattice via defects to the unreacted core surface, as seen in Figure 6b [70]; the ions within the core (i.e., metallic cations and oxygen anions) may migrate outwards across the product layer driven by the chemical-potential gradients, and enter the gas-solid surface to partner the adsorbed molecules and form vacancies [65] [1]. Besides, as the reaction proceeds, the collapse and clustering of metallic nuclei [58] as well as the growth stresses between the unreacted core and the product layer [65] may form cracks, voids and hence

---

[1] In fact, for p-type metal-deficient oxide (e.g., oxide of nickel, copper, iron), anion diffusion is slow, and usually cation diffusion dominates the transport process. In this case, “A” in Figure 6b should be replaced by “V_B” (the vacancy of B)

porous product layers, enabling gas phase diffusion and direct interactions between the gas molecules and the unreacted core, as seen in Figure 6a [71]. The diffusion mechanism by which the reactants penetrate through the product layer is complicated and strongly depends on the type of the metal, the grain configuration, the impurities, and the operating conditions.

As an estimation, the unreacted shrinking-core model (USCM) is widely used in the literature to simplify the grain diffusion process [4, 58, 65, 68, 72, 73], in which a product layer is formed around an unreacted core inside the grain, as seen in Figure 6. The gaseous reactant is assumed to diffuse through the product layer, and react with the unreacted core. The conversion process controlled by the grain diffusion can thus be modeled as:

$$-\frac{1}{\nu_r}\frac{dN_B}{dt}=-\frac{dN_A}{dt}=s_{oc}S_o\delta_{oc}D_{e,g}\frac{C_A}{\delta_{grain}-z_{un,gr}} \quad (22)$$

where δ_{grain} and $z_{\mathrm{un,gr}}$ are the thickness of the grain and the unreacted core, respectively. The effective diffusivity can be expressed in an Arrhenius form [59, 70]:

$$D_{e,g}=D_0\exp\left(-E_{e,g}/RT\right) \quad (23)$$

The pre-exponential factor, D_0, and the activation energy $E_{\mathrm{e,g}}$, can be obtained from experiments for each specific type of metal oxide. Eq. (22) can be rearranged and integrated to obtain the parabolic law of conversion as:

$$X_B^2=t/\tau_{d,g},\ \tau_{d,g}=\frac{\hat{\rho}_B\delta_{grain}}{2\nu_r s_{oc}C_A D_{e,g}} \quad (24)$$

Eq. (24) is also a simplified derivation of the famous Wagner's parabolic scaling theory [74] commonly studied in the field of metal oxdation and corrosion.

The Damköhler number for the grain diffusion is:

$$Da_{d,g} = \frac{\tilde{\rho}_s k_r \delta_{grain}}{2D_{e,g}} \quad (25)$$

Thus, thin grain layers should be used to decrease the grain diffusion resistance. In addition, higher operating temperature favors the grain diffusivity and hence increases the mass diffusion rate within the grain.

3.1.2 Support Dense Layer

The dense layer in the reactor behaves as a structure support for the porous OC layer. To minimize the thermal-stress-induced factures between the porous and the dense layers, the same support materials should be used as the binder. The outer surface of the dense layer should sustain sufficient bonding with the porous layer. The support layer should be resistant to the oxidizing and corrosive environments under high temperature, and maintain adequate toughness and mechanical strength to avoid fracturing during repeated cycles.

In the periodic stationary state, the dense layer also acts as a heat reservoir to match the heat transfer process: it absorbs and temporarily stores the thermal energy released from the reactions in the porous layer, and conducts that heat axially, and finally heats the bulk flow by convection. Large thermal inertia is required for the dense layer to minimize the temperature fluctuation and avoid localized hot spots. Approximately, we can select the size of the dense layer as:

$$c_{bulk}\dot{m}_{bulk}\Delta T_{\max} \sim \dot{W}_{th} \quad (26)$$

where c_{bulk} is the specific heat capacity of the support, $\dot{W}_{th}$ is the target thermal capacity, and $\Delta T_{\max}$ is the maximum temperature fluctuation caused by the reaction heat release. $\dot{m}_{bulk}$ is the circulation rate of the dense support solid, calculated as $\dot{m}_{bulk} = N\rho_{bulk}HA_{bulk} / \tau$, where ρ_{bulk} and A_{bulk} are the density and the cross-sectional area of the bulk layer, N is the total number of channels, and τ is the cycle period. Here, the heat redistribution via conduction is neglected, and a uniform reaction heat release is assumed within the solid phase. As an example, the design with $1MW_{th}$ and Al_2O_3 as the dense layer requires a circulation rate of 40kg s^{-1} to restrict ΔT_{max} below 20 K. As predicted by Eq. (26), a thicker dense layer and a faster spinning velocity increase the circulation rate of the solids, and hence reduce the maximum temperature fluctuation. Note that Eq.(26) tends to overestimate the temperature variation by neglecting conduction, but underestimate localized hot spots caused by non-uniform reaction heat release.

Near the reactor inlet, the cold bulk stream is heated as it enters the reactor. Within this region, a rapid temperature increase is usually observed in both the gas and solid phases, as seen in part 2, because of the relatively large temperature difference and hence high heat convection rate between the solid and gas phases, as opposed to the minimal axial temperature variation as the flow approaches the exit. In this area the reaction heat release is relatively low because of the low temperature, and thus, the energy in the solid phase is mainly balanced between convective cooling and conduction. Thus, a highly conductive dense layer is the key to effectively preheating the bulk flow. The energy balance for one cycle near the channel inlet can be expressed as:

$$A_{bulk}\frac{d}{dz}\left(k_s\frac{dT_s}{dz}\right) \approx P_c h_{gs}\left(T_s - T_g\right) \quad (27)$$

where A_{bulk}, P_c are the cross-sectional area of the solid phase, and the channel perimeter. T_s, and T_g are the temperature of the solid and gas phases. k_s, and h_{gs} are the thermal conductivity of the support substrate and the convective heat-transfer coefficient. z is the channel axial direction. Eq. (27) indicates that a thicker dense layer (A_{bulk}) with a higher thermal conductivity (k_s) sustains stronger convective cooling near the inlet, reduces the axial temperature variation of the solid, favors the preheating process, and thus enhances the solid temperature as well as the reaction rates. Some ceramic materials with good potential because of the high thermal conductivity are listed in Table 3. Note that the thermal conductivity may vary significantly with respect to the temperature, crystalline structures of the material, and the preparation method.

3.2 Design Parameters

The design of the channel determines the flow and the reaction patterns within the reactor. A small channel (d_h) with a high specific surface area (s_c) is required for the channel to provide sufficient contact between the flow and the OC, and hence, enhance the reactivities. The size of the channel (d_h) affects the mass transfer rate (h_m), as discussed in Section 3.1. On the other hand, a small channel also improves the convective cooling, i.e., h_{gs} = Nu$\cdot k_g/d_h$, where Nu is the Nussult number, leading to a lowered solid temperature and then reduced redox rates, as well as an enlarged local temperature fluctuation caused by the energy mismatch, and a larger axial temperature difference near the inlet (see Eq.(27)). In this case, a much thicker solid layer is required to provide sufficient heat for convection in the preheat zone and maintain the energy balance within the reactor. Because of these two aspects, a reasonable channel size (d_h) for the rotary CLC reactor ranges from 0.5 to 5 mm. Thus, the flow field within the channel is in general laminar.

The pressure drop within the reactor is caused by skin friction, and can be calcualted as [75], $\Delta p = \frac{1}{2} C_f u_g \mu_g H / d_h^2$, where u_g, and μ_g are the mean velocity and the dynamic viscosity of the bulk flow, C_f is the friction constant from the friction factor ($f = C_f$ / Re). For a squared-channel channel with the width of 2 mm and the height of 1 m, a 1kPa pressure drop is expected for the operation at 1000℃ and u_g of 1m/s. In general, the pressure drop is negligible as compared to the operating pressure.

The channels can be formed in a variety of geometries, e.g., grid type, honeycomb geometry shapes, plate types, etc. Different geometries of the channel are accompanied by different Sh's, Nu's, and C_f's and hence affect the mass and heat transfer processes as well as the pressure distribution. Besides, the geometry may affect the mechanical strength and alter the resistance to the stresses associated with temperature variations. The OC coating methods on the channel walls and the fabrication costs also depend on the geometry.

The sector design should provide adequate residence time for the channel in each sector. The channel residence time is determined by the rotational velocity (ω), and the size of each purging sector (θ_i), i.e., $\tau_i = \theta_i/\omega$. For the optimal design, a large fuel sector is always preferred as more fuel can be admitted into the reactor and thus a smaller reactor is needed to reach the thermal capacity (Eq.(32)). However, complete reduction of the OC should be avoided in selecting the fuel sector size, since the reduction rate may slow down as the OC is consumed and the fuel conversion in the channel drops significantly as the OC approaches full reduction. The residual metal oxide in the OC also controls carbon deposition risk in the fuel sector. Thus, the size of the fuel sector should satisfy:

$\tau_{fuel} = \theta_{fuel}/\omega \ \leq \tau_{\text{full-red}}$ (28)

On the other hand, the size of the air sector should be large enough such that the OC on the walls are sufficiently exposed to and re-oxidized by the flowing air. Complete oxidation of the OC may not be necessary due to the fact that the oxidation rate may decrease significantly as the OC approaches complete oxidation state, as noted in Part 2. In addition, the catalytic effects of the metal in the OC layer may help enhance the adsorption and dissociation of the fuel molecules on the grain lattice and hence improve the reduction rate in the following fuel sector, as discussed in Section 3.1. Thus, it is reasonable to maintain a certain amount of OC unconverted in the OC layer at the end of the air sector. The size of the air sector should be selected such that:

$\tau_{\text{air}} = \theta_{\text{air}}/\omega \geq \tau_{\text{sufficient-ox}}$ (29)

$\tau_{\text{full-red}}$, and $\tau_{\text{sufficient-ox}}$ are mainly controlled by the redox characteristics of the OC under specific operating conditions.

To ensure separation of CO_2 and avoid dilution of air, the residence time of channels (τ_i) in each purging sector should be kept adequately longer than that for steam (t_i) to purge through the channel:

$\tau_i = \theta_{\text{i}}/\omega > t_i$, i = *fuel purge* or *air purge* (30)

where t_{i} is determined by Eq. (2). Therefore, the choice of the purge sector sizes (θ_{i}) is usually coupled with the selection of the purge velocity and the channel height. As discussed in Section 2.2, one can reduce the purging volume (θ_i) by increasing the steam velocities while maintaining a constant rotational speed. This is usually the case for the air purging sector where we minimize the purging volume by admitting a fast stream. However, the steam velocity in the fuel purge sector is usually constrained in order to oxidize all the residual fuel within the channel. Thus, in the case with low reduction reactivity, the purge volume can be much larger (see the iron-based case in Part 2).

For the rotary design with different OCs, the rate-limiting step varies, and thus the size requirements of each sector differ accordingly. For instance, as showed in Part 2, the nickel-based design has a much larger air sector owing to its slow oxidation rate; the longer gas residence time needed for fuel conversion requires a much larger share of fuel purge sector in the iron-based design for separation; for copper-based design, the size of the fuel sector takes the majority of the reactor and it is constrained by the full reduction of the OC.

The height of the reactor is selected to ensure fuel conversion:

$H \geq (1+\kappa)\, z_{99\%}$ (31)

where $z_{99\%}$ is the height required to reach 99% fuel conversion, and κ is the redundancy factor. Generally, a 25% redundancy is required to account for the uncertainties with the operations. The diameter of the reactor is determined to reach the target thermal capacity:

$$\frac{1}{8}\theta_{fuel} D^2 \dot{n}_f \Delta h_r = \dot{W}_{th} \quad (32)$$

Here D is diameter of the rotary wheel, Δh_r is the enthalpy of reaction of the fuel, and $\dot{n}_f$ is the flow rate in the feed chamber. Eq. (32) shows that the thermal capacity of the reactor scales with the square of the diameter. The height of the reactor remains unchanged with the up-scaling.

3.3 **Operating Condition**

The operating temperature is one of the most important factors for the overall performances of the rotary reactor. The inlet (T_{in}) and the exit (T_{ex}) temperatures of the rotary reactor are selected on the basis of the characteristics of the OCs and the compatibility requirements from the power generation system. As discussed previously, a higher operating temperature always enhances the redox rates, improves the fuel conversion, and reduces the size of the reactor and the costs of fabrication. From the system perspective, a higher temperature corresponds to a higher turbine inlet temperature (TIT), which leads to a higher net plant efficiency. However, the inlet temperature of the bulk flow is constrained by the capability of the preheating units in the system, as discussed in Section 2.4. The selection of the exit temperature from the reactor is mainly controlled by the material limits from the OCs and the gas turbine. For the state-of-the-art gas turbines used in the conventional power plants, the TIT can be 1400 ℃ or above [76]. It is worth noting that for fluidized CLC reactor with OCs in the form of particles, the operating temperatures are usually constrained below 1200℃ [4], because of the concerns with agglomeration and defluidization. In contrast, these concerns are less significant for the rotary reactor because of the regulated flow patterns through the reactor and the limited temperature variations in the cyclic operations. Thus, a reasonable operating temperature for rotary CLC reactor is in the range of 1000-1400℃. Similar inlet temperatures are recommended for the feed streams to reduce the thermal stresses in the reactor, which on the other hand may lead to a more complex system design and higher operational cost.

The operating pressure (P) is also critical in determining the functionality of the reactor. In general, the pressure is determined by the requirements from the power generation system, with the consideration of the net plant efficiency, the system specific work output and the CO_2

compression. A reasonable operating pressure ranges from 10-40atm. The pressure affects the reaction rates by changing the gas concentration, the diffusion and adsorption processes. The reaction rate may increase with a higher total pressure because of the increase in reactant concentration, as reported by ref. [77-79]. On the other hand, the decrease in the molecular diffusivity at the high pressure (Eq.(9)) may increase the external and internal mass diffusion resistances and thus inhibit the reaction rates. The amount of the available open sites on the grain lattice may decrease at elevated pressures, as discussed in Appendix B, which leads to a lower reaction rate. Besides, the operating pressure also influences the heat convection by changing the density and hence the thermal inertia of the streams.

The feed stream in the fuel sector is usually diluted by recirculated CO_2 to control the fuel feed rate in the channel and lower the operating temperature. The fuel concentration ($x_{\mathrm{fuel},0}$) at the inlet affects the reduction rate, as expressed in Eq. (6), and changes the reactor height required to convert the fuel (Eq. (31)). One can always reduce the reactor height by using a higher fuel concentration and a low flow velocity, as pointed out in Section 2.1. However, the fuel stream with high concentration near the inlet rapidly consumes the available OCs, leading to a shortened reduction period (Eq.(28)), and hence an enlarged reactor size (Eq.(32)). A large fuel purge sector is also necessary in this case because a longer residence time of the gas is needed to consume the residual fuel in the channel. Thus, the height of the reactor is reduced at the cost of an enlarged reactor diameter. The optimal choice depends on the tradeoff effects and it differs with the selection of the OC.

The rotational velocity (ω) controls the cycle period (τ). A faster rotational speed is preferred to increase the admitted fuel flow rate (Eq. (3)), reduce the temperature fluctuation (Eq. (26)), decrease the carbon deposition risk and maintain the fast reduction reactivity (Eq. (28)). On the other hand, sufficient residence time is required for complete residual gas cleaning (Eq. (30)) and the OC regeneration (Eq. (29)). Therefore, the choice of the rotational velocity is to minimize the cycle period while maintain long enough residence time for each channel in the purge sectors and the air sector.

The feed velocity (u_{fuel}) in the fuel sector determines the residence time of gas and hence the required height ($z_{99\%}$) for complete fuel conversion (Eq.(1)). A higher feed velocity reduces the diameter of the reactor by increasing the feed rate of the fuel (Eq. (32)) but requires a longer reactor height ($z_{99\%}$) to convert the fuel. The selection of the fuel velocity is usually related to that of the fuel concentration at the inlet, as discussed previously, and these two parameters should be determined together to reach high fuel feed rate and maintain a reasonable reactor height for fuel conversion. The fuel purge velocity ($u_{\mathrm{fuel,p}}$) is then selected accordingly to provide a similar flow field within the channel to completely convert the residual fuel. As a result, for the design with a slow fuel velocity, a low purge rate should be used in the following purge sector, leading to a larger share of the fuel purge sector required for separation (Eq. (30)). In contrast, the steam velocity in the air purge sector ($u_{\mathrm{air,p}}$) can be much higher, as pointed out in Section 2.2, and thus, the air purge sector can be much smaller.

The air feed velocity (u_{air}) is mainly determined by the overall heat balance:

$$\theta_{air}\rho u_{air}c_p\left(T_{ex}-T_{in}\right) \approx \theta_{fuel}\dot{n}_f\Delta h_r \quad (33)$$

where ρ and c_p are the density and the specific heat capacity of the air stream. Sufficient air stream is required to transfer the reaction heat and maintain the operating temperature. The air feed velocity also affects the oxygen concentration within the reactor and thus affects the characteristic time for re-oxidation ($\tau_{sufficient\text{-}ox}$). Thus, u_{air} and θ_{air} should be determined simultaneously on the basis of Eqs. (29) and (33).

4. Design Procedure

The design procedure (Figure 7) is based on the relative importance and the dependent relationships of the design parameters, as discussed in Section 3.

As showed in Figure 7, the design input includes the target thermal capacity ($\dot{W}_{th}$), the type of the fuel, the operating temperatures (T_{in}, T_{ex}) and the pressure (P), and the type of the metal oxide. The design input data are determined by the compatibility requirements from the system integration. The chemical and thermal properties of the metal oxide must allow continuous cycling in the reactor at the operating temperature and pressures without melting, fouling, and decomposition.

The OC design and the preparation techniques are then determined to provide sufficient reduction and oxidation rates. A thick OC layer (δ_{oc}) with large active surface areas (s_{oc}) leads to a higher consumption rate of the fuel (Eqs. (3) and (5)). On the other hand, δ_{oc} is constrained to minimize the mass transfer resistance caused by the external and internal diffusion within the porous layer (Eqs. (10) and (15)). A highly porous (ε) OC layer improves the gas permeability through the pores (Eq. (13)) and thin grain layers (δ_{grain}) on the porous substrate enhances the diffusion through the product layer in the lattice (Eq. (25)). An intermediate range of the OC conversion (ΔX_{oc}) is preferred to maintain fast redox rates during the cyclic operation (Eq. (21)) and eliminate the carbon deposition risk, while a sufficient oxygen transport capacity (R_{oc}) is required for full fuel consumption (Eq. (3)). The selection of the support material and the design of the dense layer should provide sufficient thermal inertia and conductivity to minimize the temperature fluctuation (Eq.(26)) and maintain reasonable isothermality of the reactor (Eq. (27)). The support material should also be stable and resistant to corrosion and thermal distortion.

The choice for the channel design is based on the redox reactivities of the OC, the flow pattern required for the reaction, the dimensions of the OC layer and the dense support layer. A sufficiently large channel should be utilized to accommodate both layers, maintain high temperature near the inlet (Eq. (27)), and reduce the pressure drop along the reactor. On the other hand, the channel width is constrained below a certain value to reduce the external mass diffusion resistance (Eq.(10)). The geometry of the channel affects the mechanical stability as well as the fabrication costs of the reactor.

The operating conditions in the fuel and the fuel purge sectors are then selected on the basis of the reduction kinetics of the OC. The reactor height ($z_{99\%}$) for fuel conversion is an important indicator for the choice of the feed fuel concentration ($x_{\mathrm{fuel},0}$) and the flow velocity (u_{fuel}). With the same amount of fuel admitted, $z_{99\%}$ decreases with the increase of the fuel concentration at the inlet, which on the other hand may lead to a shorter reduction time in the fuel sector before complete reduction occurs. A similar velocity ($u_{\mathrm{fuel,p}}$) should be used in the fuel purge sector to completely oxidize the residual fuel. The reactor height can then be selected based on $z_{99\%}$ with sufficient redundancy (Eq. (31)).

The channel residence time in the fuel sector (τ_{fuel}) is constrained by the characteristic time for complete reduction (Eq.(28)). The choices for the size (τ_{air}) and the feed flow rate (u_{air}) of the air sector are governed by the overall energy balance of the reactor (Eq.(33)) and the residence time required to reach sufficient OC regeneration (Eq. (29)). Depending on the reactor height and the steam velocity, the necessary size of the purge sectors ($\tau_{fuel,p}$ or $\tau_{air,p}$) can then be selected (Eq. (30)). The rotational velocity (ω) and the share of each sector (θ_i) are then selected according to τ_{fuel}, τ_{air}, $\tau_{fuel,p}$ and $\tau_{air,p}$. A higher steam rate ($u_{air,p}$) is recommended in the air purge sector to minimize $\theta_{air,p}$. Finally, the diameter of the reactor can be determined on the basis of the fuel feed rate and the target thermal capacity (Eq. (32)).

5. Conclusion

In this work, the design fundamentals of a novel rotary CLC reactor with micro-channel structures are examined in details. The primary design objectives and criteria of the rotary reactor have been proposed, including the requirements on fuel conversion, CO_2 separation, operational stabilities, the integration and the economic feasibility in a power generation system. For each of the objective, the key parameters that control the performance are identified.

To achieve the design objectives, a variety of parameters can be determined, including material selection, reactor geometry and arrangement, and the operating conditions. All of these parameters are highly coupled, and strongly affect the performance of the reactor. A thorough discussion of the design fundamentals is presented in this study, which provides insights to the design optimization:

- The quality of the OC is the most important design factor. A suitable OC exhibits high redox rates and maintains stability in repeated cycles. The redox of the OC involves multiple intermediate steps, and the key parameters are identified. A thick dense support layer with high thermal inertia and conductivity is necessary to maintain the stability of the reactor.
- The design of the channel influences the heat and the mass transfer between the bulk flow and the OC. The sizes of the different sectors are governed by the characteristic time for reduction, oxidation, and purging. The dimensions of the reactor are controlled by fuel conversion and the thermal output.
- The pressure and temperature are the most important operating parameters and they are determined by the compatibility requirement from the system integration. The inlet concentration and the flow rate in fuel sector directly control the height of the reactor while the air flow rate in the air sector determines the overall heat balance. The feed velocities in purge sectors are determined to ensure complete CO_2 separation.

The design procedure has been proposed on the basis of the influences, the relative importance, and the dependent relationships of the design parameters with respect to the performance of the rotary reactor. Part 2 presents the application of this methodology to the design of three commonly used OCs, i.e., nickel, copper, and iron, and evaluates the behaviors of the rotary reactor using numerical simulations.

Acknowledgement

This study is financially supported by a grant from the MASDAR Institute of Science and Technology and the King Abdullah University of Science and Technology (KAUST) Investigator Award.

Reference

[1] H.J. Richter, K.F. Knoche, Reversibility of combustion processes., in: ACS Symposium Series, 1983, pp. 71-85.
[2] A. Lyngfelt, B. Leckner, T. Mattisson, A fluidized-bed combustion process with inherent CO_2 separation; application of chemical-looping combustion, Chem. Eng. Sci., 56 (2001) 3101-3113.
[3] M.M. Hossain, H.I. de Lasa, Chemical-looping combustion (CLC) for inherent CO_2 separations - a review, Chem. Eng. Sci., 63 (2008) 4433-4451.
[4] J. Adanez, A. Abad, F. Garcia-Labiano, P. Gayan, L.F. de Diego, Progress in Chemical-Looping Combustion and Reforming technologies, Progress in Energy and Combustion Science, 38 (2012) 215-282.
[5] M. Johansson, T. Mattisson, A. Lyngfelt, Use of $NiO/NiAl_2O_4$ Particles in a 10 kW Chemical-Looping Combustor, Ind. Eng. Chem. Res., 45 (2006) 5911-5919.
[6] C. Linderholm, A. Abad, T. Mattisson, A. Lyngfelt, 160 h of chemical-looping combustion in a 10 kW reactor system with a NiO-based oxygen carrier, Int. J. Greenhouse Gas Control, 2 (2008) 520-530.
[7] A. Abad, T. Mattisson, A. Lyngfelt, M. Ryden, Chemical-looping combustion in a 300W continuously operating reactor system using a manganese-based oxygen carrier, Fuel, 85 (2006) 1174-1185.
[8] N. Berguerand, A. Lyngfelt, Design and operation of a 10kWth chemical-looping combustor for solid fuels - Testing with South African coal, Fuel, 87 (2008) 2713-2726.
[9] J. Adanez, P. Gayan, J. Celaya, L.F. de Diego, F. Garcia-Labiano, A. Abad, Chemical Looping Combustion in a 10 kWth Prototype Using a CuO/Al_2O_3 Oxygen Carrier: Effect of Operating Conditions on Methane Combustion, Ind. Eng. Chem. Res., 45 (2006) 6075-6080.
[10] D.L.F. de, F. Garcia-Labiano, P. Gayan, J. Celaya, J.M. Palacios, J. Adanez, Operation of a 10 kWth chemical-looping combustor during 200 h with a CuO-Al2O3 oxygen carrier, Fuel, 86 (2007) 1036-1045.
[11] C. Dueso, F. Garcia-Labiano, J. Adanez, D.L.F. de, P. Gayan, A. Abad, Syngas combustion in a chemical-looping combustion system using an impregnated Ni-based oxygen carrier, Fuel, 88 (2009) 2357-2364.
[12] P. Kolbitsch, J. Bolhar-Nordenkampf, T. Proell, H. Hofbauer, Operating experience with chemical looping combustion in a 120 kW dual circulating fluidized bed (DCFB) unit, Int. J. Greenhouse Gas Control, 4 (2010) 180-185.
[13] P. Kolbitsch, T. Proell, J. Bolhar-Nordenkampf, H. Hofbauer, Design of a chemical looping combustor using a dual circulating fluidized bed reactor system, Chem. Eng. Technol., 32 (2009) 398-403.
[14] L. Shen, J. Wu, Z. Gao, J. Xiao, Reactivity deterioration of NiO/Al2O3 oxygen carrier for chemical looping combustion of coal in a 10 kWth reactor, Combust. Flame, 156 (2009) 1377-1385.
[15] H. Gu, L. Shen, J. Xiao, S. Zhang, T. Song, Chemical Looping Combustion of Biomass/Coal with Natural Iron Ore as Oxygen Carrier in a Continuous Reactor, Energy Fuels, 25 (2011) 446-455.
[16] F. Li, L. Zeng, L.G. Velazquez-Vargas, Z. Yoscovits, L.-S. Fan, Syngas chemical looping gasification process: bench-scale studies and reactor simulations, AIChE J., 56 (2010) 2186-2199.
[17] L.S. Fan, Chemical looping systems for fossil energy conversions., John Wiley & Sons, Inc, Hoboken, New Jersey, 2010.
[18] S. Noorman, M. van Sint Annaland, H. Kuipers, Packed Bed Reactor Technology for Chemical-Looping Combustion, Ind. Eng. Chem. Res., 46 (2007) 4212-4220.
[19] S. Noorman, F. Gallucci, M. van Sint Annaland, J.A.M. Kuipers, Experimental Investigation of Chemical-Looping Combustion in Packed Beds: A Parametric Study, Ind. Eng. Chem. Res., 50 (2011) 1968-1980.
[20] I.M. Dahl, E. Bakken, Y. Larring, A.I. Spjelkavik, S.F. Håkonsen, R. Blom, On the development of novel reactor concepts for chemical looping combustion, Energy Procedia, 1 (2009) 1513-1519.
[21] S.F. Håkonsen, R. Blom, Chemical Looping Combustion in a Rotating Bed Reactor – Finding Optimal Process Conditions for Prototype Reactor, Environmental Science & Technology, 45 (2011) 9619-9626.
[22] Z. Zhao, T. Chen, A.F. Ghoniem, Rotary Bed Reactor for Chemical-Looping Combustion with Carbon Capture. Part 1: Reactor Design and Model Development, Energy & Fuels, 27 (2013) 327-343.
[23] Z. Zhao, Rotary bed reactor for chemical-looping combustion with carbon capture, in: Dept. of Mechanical Engineering, Massachusetts Institute of Technology, Cambridge, 2012.
[24] D. Pavone, CO_2 capture by means of chemical looping combustion., in: Proceedings of the COMSOL Multiphysics User's Conference., Paris, France, 2005.

[25] D. Pavone, M. Rolland, E. Lebas, CO_2 capture using chemical looping combustion for gas turbine application., in: Proceedings of 8th International Conference of Greenhouse Gas Control Technologies (GHGT-8). Trondheim, Norway, 2006.
[26] Z. Zhao, T. Chen, A.F. Ghoniem, Rotary Bed Reactor for Chemical-Looping Combustion with Carbon Capture. Part 2: Base Case and Sensitivity Analysis, Energy & Fuels, 27 (2013) 344-359.
[27] Z. Zhao, A.F. Ghoniem, Design of a Rotary Reactor for Chemical-looping Combustion. Part 2: Comparison of Copper-, Nickel-, and Iron-based Oxygen Carriers., Submitted to Fuel for publication, (2013).
[28] F.E. Aslan-zada, V.A. Mammadov, F. Dohnal, Brush seals and labyrinth seals in gas turbine applications, Proceedings of the Institution of Mechanical Engineers, Part A: Journal of Power and Energy, 227 (2013) 216-230.
[29] P. Cho, T. Mattisson, A. Lyngfelt, Carbon Formation on Nickel and Iron Oxide-Containing Oxygen Carriers for Chemical-Looping Combustion, Ind. Eng. Chem. Res., 44 (2005) 668-676.
[30] H. Jin, T. Okamoto, M. Ishida, Development of a Novel Chemical-Looping Combustion: Synthesis of a Solid Looping Material of $NiO/NiAl_2O_4$, Ind. Eng. Chem. Res., 38 (1999) 126-132.
[31] M. Ishida, H. Jin, T. Okamoto, Kinetic behavior of solid particle in chemical-looping combustion: suppressing carbon deposition in reduction, Energy Fuels, 12 (1998) 223-229.
[32] H. Jin, M. Ishida, Reactivity Study on Natural-Gas-Fueled Chemical-Looping Combustion by a Fixed-Bed Reactor, Ind. Eng. Chem. Res., 41 (2002) 4004-4007.
[33] A. Hoteit, M.K. Chandel, A. Delebarre, Nickel- and copper-based oxygen carriers for chemical looping combustion, Chem. Eng. Technol., 32 (2009) 443-449.
[34] M.K. Chandel, A. Hoteit, A. Delebarre, Experimental investigation of some metal oxides for chemical looping combustion in a fluidized bed reactor, Fuel, 88 (2009) 898-908.
[35] T. Mattisson, M. Johansson, A. Lyngfelt, The use of NiO as an oxygen carrier in chemical-looping combustion, Fuel, 85 (2006) 736-747.
[36] E. Jerndal, T. Mattisson, A. Lyngfelt, Thermal analysis of chemical-looping combustion, Chem. Eng. Res. Des., 84 (2006) 795-806.
[37] O. Brandvoll, Chemical looping combustion: Fuel conversion with inherent carbon dioxide capture, in, 2005, pp. No pp., given.
[38] R. Naqvi, Analysis of Natural Gas-Fired Power Cycles with Chemical Looping Combustion for CO_2 Capture., in, Norwegian University of Science and Technology, 2006.
[39] R.J. Kee, B.B. Almand, J.M. Blasi, B.L. Rosen, M. Hartmann, N.P. Sullivan, H. Zhu, A.R. Manerbino, S. Menzer, W.G. Coors, J.L. Martin, The design, fabrication, and evaluation of a ceramic counter-flow microchannel heat exchanger, Applied Thermal Engineering, 31 (2011) 2004-2012.
[40] Y. Wang, A.L. Tonkovich, T. Mazanec, F.P. Daly, D. VanderWiel, J. Hu, C. Cao, C. Kibby, X.S. Li, M.D. Briscoe, Fischer-tropsch synthesis using microchannel technology and novel catalyst and microchannel reactor, U.S. Patent No. 7,084,180. 1. Aug. 2006., in.
[41] J. Adanez, L.F. de Diego, F. Garcia-Labiano, P. Gayan, A. Abad, J.M. Palacios, Selection of Oxygen Carriers for Chemical-Looping Combustion, Energy Fuels, 18 (2004) 371-377.
[42] M. Johansson, T. Mattisson, A. Lyngfelt, A. Abad, Using continuous and pulse experiments to compare two promising nickel-based oxygen carriers for use in chemical-looping technologies, Fuel, 87 (2008) 988-1001.
[43] P. Gayan, L.F. de Diego, F. Garcia-Labiano, J. Adanez, A. Abad, C. Dueso, Effect of support on reactivity and selectivity of Ni-based oxygen carriers for chemical-looping combustion, Fuel, 87 (2008) 2641-2650.
[44] P. Cho, T. Mattisson, A. Lyngfelt, Comparison of iron-, nickel-, copper- and manganese-based oxygen carriers for chemical-looping combustion, Fuel, 83 (2004) 1215-1225.
[45] L.F. de Diego, F. Garcia-Labiano, J. Adanez, P. Gayan, A. Abad, B.M. Corbella, J.M. Palacios, Development of Cu-based oxygen carriers for chemical-looping combustion, Fuel, 83 (2004) 1749-1757.
[46] B.M. Corbella, L. de Diego, F. Garcia, J. Adanez, J.M. Palacios, The Performance in a Fixed Bed Reactor of Copper-Based Oxides on Titania as Oxygen Carriers for Chemical Looping Combustion of Methane, Energy Fuels, 19 (2005) 433-441.
[47] F. Garcia-Labiano, J. Adanez, L.F. de Diego, P. Gayan, A. Abad, Effect of Pressure on the Behavior of Copper-, Iron-, and Nickel-Based Oxygen Carriers for Chemical-Looping Combustion, Energy Fuels, 20 (2006) 26-33.
[48] S.Y. Chuang, J.S. Dennis, A.N. Hayhurst, S.A. Scott, Development and performance of Cu-based oxygen carriers for chemical-looping combustion, Combust. Flame, 154 (2008) 109-121.

[49] M. Johansson, T. Mattisson, A. Lyngfelt, Investigation of Fe_2O_3 with $MgAl_2O_4$ for Chemical-Looping Combustion, Ind. Eng. Chem. Res., 43 (2004) 6978-6987.
[50] T. Mattisson, M. Johansson, A. Lyngfelt, Multicycle Reduction and Oxidation of Different Types of Iron Oxide Particles-Application to Chemical-Looping Combustion, Energy Fuels, 18 (2004) 628-637.
[51] M. Ryden, E. Cleverstam, M. Johansson, A. Lyngfelt, T. Mattisson, Fe_2O_3 on Ce-, Ca-, or Mg-stabilized ZrO_2 as oxygen carrier for chemical-looping combustion using NiO as additive, AIChE J., 56 (2010) 2211-2220.
[52] F. Garcia-Labiano, L.F. de Diego, J. Adanez, A. Abad, P. Gayan, Reduction and Oxidation Kinetics of a Copper-Based Oxygen Carrier Prepared by Impregnation for Chemical-Looping Combustion, Ind. Eng. Chem. Res., 43 (2004) 8168-8177.
[53] C.R. Forero, P. Gayán, F. García-Labiano, L.F. de Diego, A. Abad, J. Adánez, High temperature behaviour of a CuO/γAl2O3 oxygen carrier for chemical-looping combustion, International Journal of Greenhouse Gas Control, 5 (2011) 659-667.
[54] P. Gayán, C.R. Forero, A. Abad, L.F. de Diego, F. García-Labiano, J. Adánez, Effect of Support on the Behavior of Cu-Based Oxygen Carriers during Long-Term CLC Operation at Temperatures above 1073 K, Energy & Fuels, 25 (2011) 1316-1326.
[55] E. Jerndal, T. Mattisson, A. Lyngfelt, Investigation of Different $NiO/NiAl_2O_4$ Particles as Oxygen Carriers for Chemical-Looping Combustion, Energy Fuels, 23 (2009) 665-676.
[56] J. Adanez, F. Garcia-Labiano, D.L.F. de, P. Gayan, J. Celaya, A. Abad, Nickel-Copper Oxygen Carriers To Reach Zero CO and H2 Emissions in Chemical-Looping Combustion, Ind. Eng. Chem. Res., 45 (2006) 2617-2625.
[57] L.F. de Diego, P. Gayan, F. Garcia-Labiano, J. Celaya, A. Abad, J. Adanez, Impregnated CuO/Al2O3 Oxygen Carriers for Chemical-Looping Combustion: Avoiding Fluidized Bed Agglomeration, Energy Fuels, 19 (2005) 1850-1856.
[58] J.T. Richardson, R.M. Scates, M.V. Twigg, X-ray diffraction study of the hydrogen reduction of NiO/α-Al2O3 steam reforming catalysts, Applied Catalysis A: General, 267 (2004) 35-46.
[59] T.L. Ward, T. Dao, Model of hydrogen permeation behavior in palladium membranes, Journal of Membrane Science, 153 (1999) 211-231.
[60] E.N. Fuller, P.D. Schettler, J.C. Giddings, New method for prediction of binary gas-phase diffusion coefficients, Ind. Eng. Chem, 58 (1966) 18-27.
[61] N. Wakao, J.M. Smith, Diffusion in catalyst pellets, Chemical Engineering Science, 17 (1962) 825-834.
[62] E.E. Peterson, Chemical reaction analysis, in, Prentice-Hall, Engelwood Cliffs, New Jersey, 1965.
[63] Y. Liu, X. Tan, K. Li, Mixed Conducting Ceramics for Catalytic Membrane Processing, Catalysis Reviews, 48 (2006) 145-198.
[64] M.M. Hossain, H.I. de Lasa, Reactivity and stability of Co-Ni/Al2O3 oxygen carrier in multicycle CLC, AIChE Journal, 53 (2007) 1817-1829.
[65] N. Birks, G.H. Meier, F.S. Pettit, Introduction to the High Temperature Oxidation of Metals, Cambridge University Press, 2006.
[66] M.M. Hossain, H.I. de Lasa, Reduction and oxidation kinetics of Co-Ni/Al2O3 oxygen carrier involved in a chemical-looping combustion cycles, Chem. Eng. Sci., 65 (2010) 98-106.
[67] J. Bandrowski, C.R. Bickling, K.H. Yang, O.A. Hougen, Kinetics of the reduction of nickel oxide by hydrogen, Chemical Engineering Science, 17 (1962) 379-390.
[68] J. Szekely, J. Evans, H. Sohn, Gas-solid reactions., Academic Press, New York, NY, 1976.
[69] J.T. Richardson, M. Lei, B. Turk, K. Forster, M.V. Twigg, Reduction of model steam reforming catalysts: NiO/α-Al2O3, Applied Catalysis A, General, 110 (1994) 217-237.
[70] J. Hong, P. Kirchen, A.F. Ghoniem, Numerical simulation of ion transport membrane reactors: Oxygen permeation and transport and fuel conversion, Journal of Membrane Science, 407–408 (2012) 71-85.
[71] P. Sarrazin, A. Galerie, J. Fouletier, H. Evans, Mechanisms Of High Temperature Corrosion: A Kinetic Approach, Distributed worldwide byTrans Tech Publications Limited, 2008.
[72] T. Hidayat, M.A. Rhamdhani, E. Jak, P.C. Hayes, The Kinetics of Reduction of Dense Synthetic Nickel Oxide in H2-N2 and H2-H2O Atmospheres, Metall and Materi Trans B, 40 (2009) 1-16.
[73] F. Garcia-Labiano, L.F. de Diego, J. Adanez, A. Abad, P. Gayan, Temperature variations in the oxygen carrier particles during their reduction and oxidation in a chemical-looping combustion system, Chem. Eng. Sci., 60 (2005) 851-862.

[74] C. Wagner, Beitrag zur Theorie des Anlaufsvorgangs,, Z Phys. Chem, , (1933) 25-41.
[75] A.F. Mills, Heat Transfer (2nd Edition), Prentice Hall, Englewood Cliffs, New Jersey, 1998.
[76] A.F. Ghoniem, Needs, resources and climate change: Clean and efficient conversion technologies, Progress in Energy and Combustion Science, 37 (2011) 15-51.
[77] R. Siriwardane, J. Poston, K. Chaudhari, A. Zinn, T. Simonyi, C. Robinson, Chemical-Looping Combustion of Simulated Synthesis Gas Using Nickel Oxide Oxygen Carrier Supported on Bentonite, Energy Fuels, 21 (2007) 1582-1591.
[78] H. Jin, M. Ishida, A new type of coal gas fueled chemical-looping combustion, Fuel, 83 (2004) 2411-2417.
[79] G. Wu, W.A. Sirignano, F.A. Williams, Simulation of transient convective burning of an n-octane droplet using a four-step reduced mechanism, Combustion and Flame, 158 (2011) 1171-1180.
[80] NIST Standard Reference Database Number 69, webbook.nist.gov/chemistry, accessed 12/2011.
[81] E.K. Sichel, R.E. Miller, M.S. Abrahams, C.J. Buiocchi, Heat capacity and thermal conductivity of hexagonal pyrolytic boron nitride, Physical Review B, 13 (1976) 4607-4611.
[82] R.W. Powell, C.Y. Ho, P.E. Liley, Thermal Conductivity of Selected Materials, in: National Standard Reference Data Series, NSRDS-NBS 8, 1966.
[83] G.A. Slack, R.A. Tanzilli, R.O. Pohl, J.W. Vandersande, The intrinsic thermal conductivity of AIN, Journal of Physics and Chemistry of Solids, 48 (1987) 641-647.
[84] G.A. Slack, Nonmetallic crystals with high thermal conductivity, Journal of Physics and Chemistry of Solids, 34 (1973) 321-335.
[85] J.F. Shackelford, W. Alexander, J.S. Park, CRC materials science and engineering handbook, CRC Press, 1994.
[86] V.K. Chakravarthy, C.S. Daw, J.A. Pihl, Thermodynamic analysis of alternative approaches to chemical looping combustion, Energy Fuels, 25 (2011) 656-669.
[87] N.R. McGlashan, Chemical-looping combustion - a thermodynamic study, Proc. Inst. Mech. Eng., Part C, 222 (2008) 1005-1019.

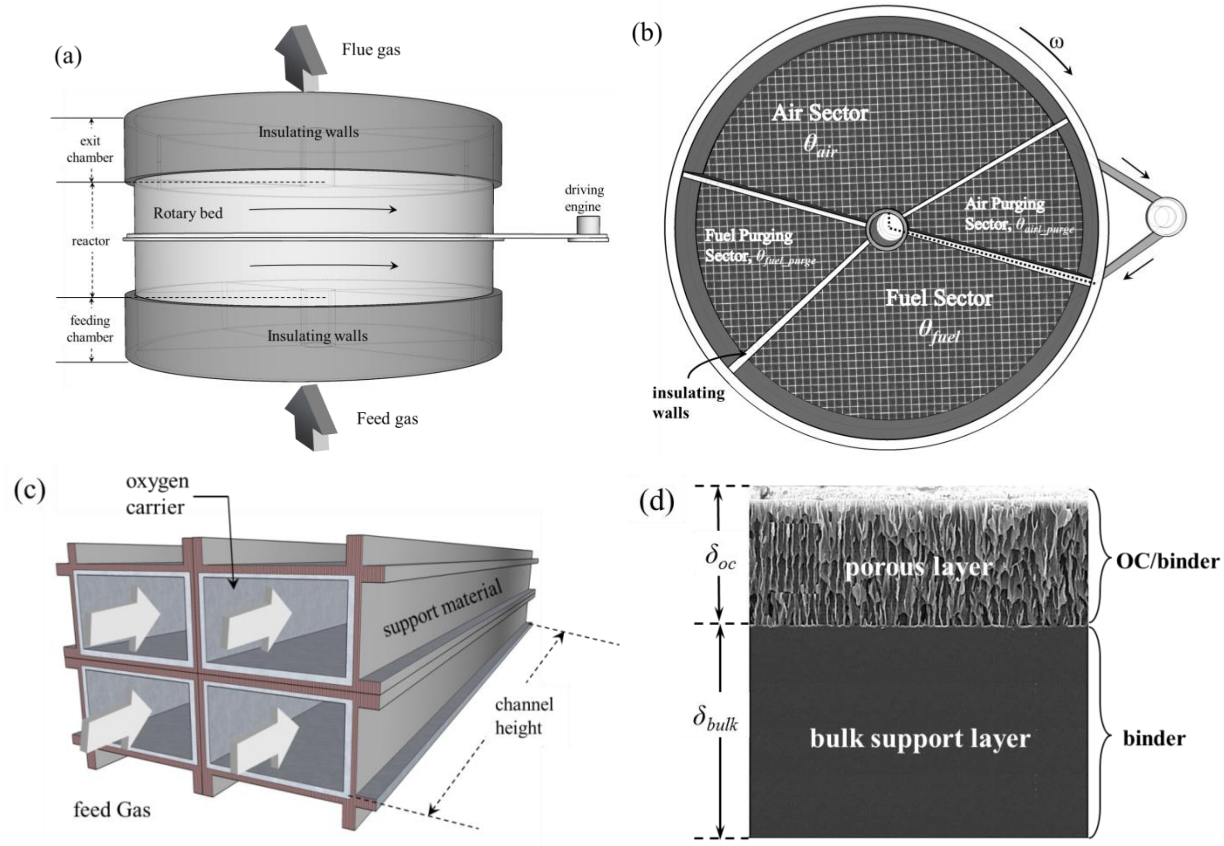

Figure 1. Schematic diagram of rotary CLC system design[22]: (a) front view, (b) bottom view, (c) individual channel structure, and (d) the oxygen carrier coated on the surface.

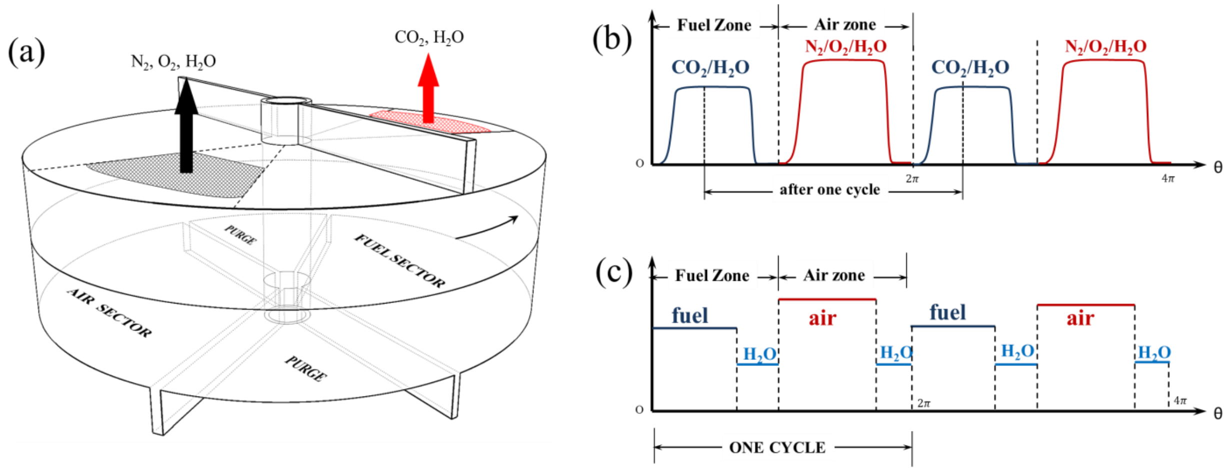

Figure 2 Schematic illustrations of the reactor with inlet and exit flue streams. Panel (a) is the isometric projection of the reactor, and panels (b) and (c) are the gas species concentration at the exit and the inlet of the reactor for two cycles.

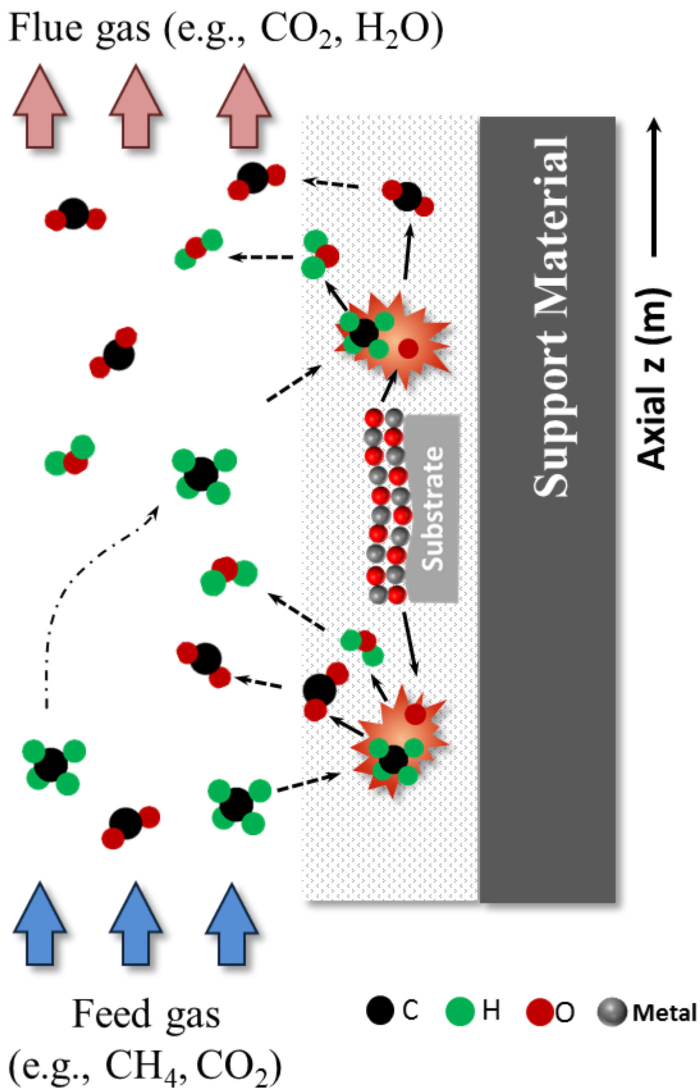

Figure 3 Schematic drawing of the reactive flow in the channel.

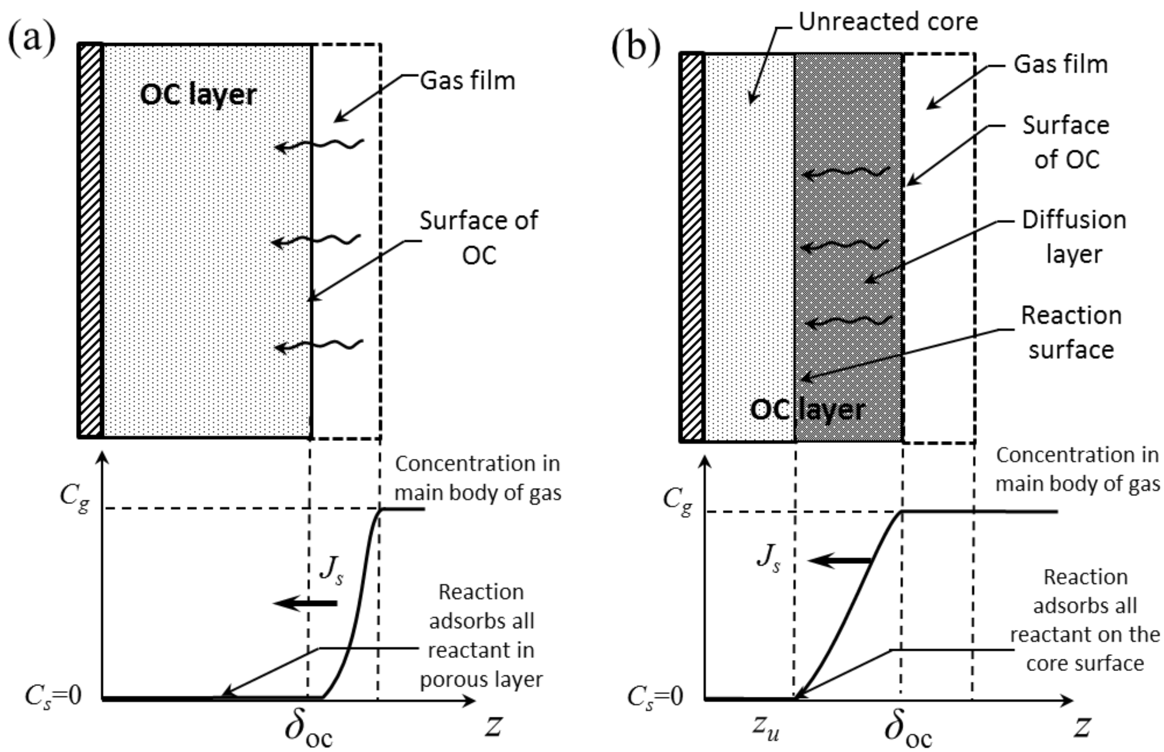

Figure 4 Schematic illustrations of the reacting OC under the control of (a) the external diffusion, (b) the internal diffusion. The reactant is fuel (or air) for the reduction (or oxidation).

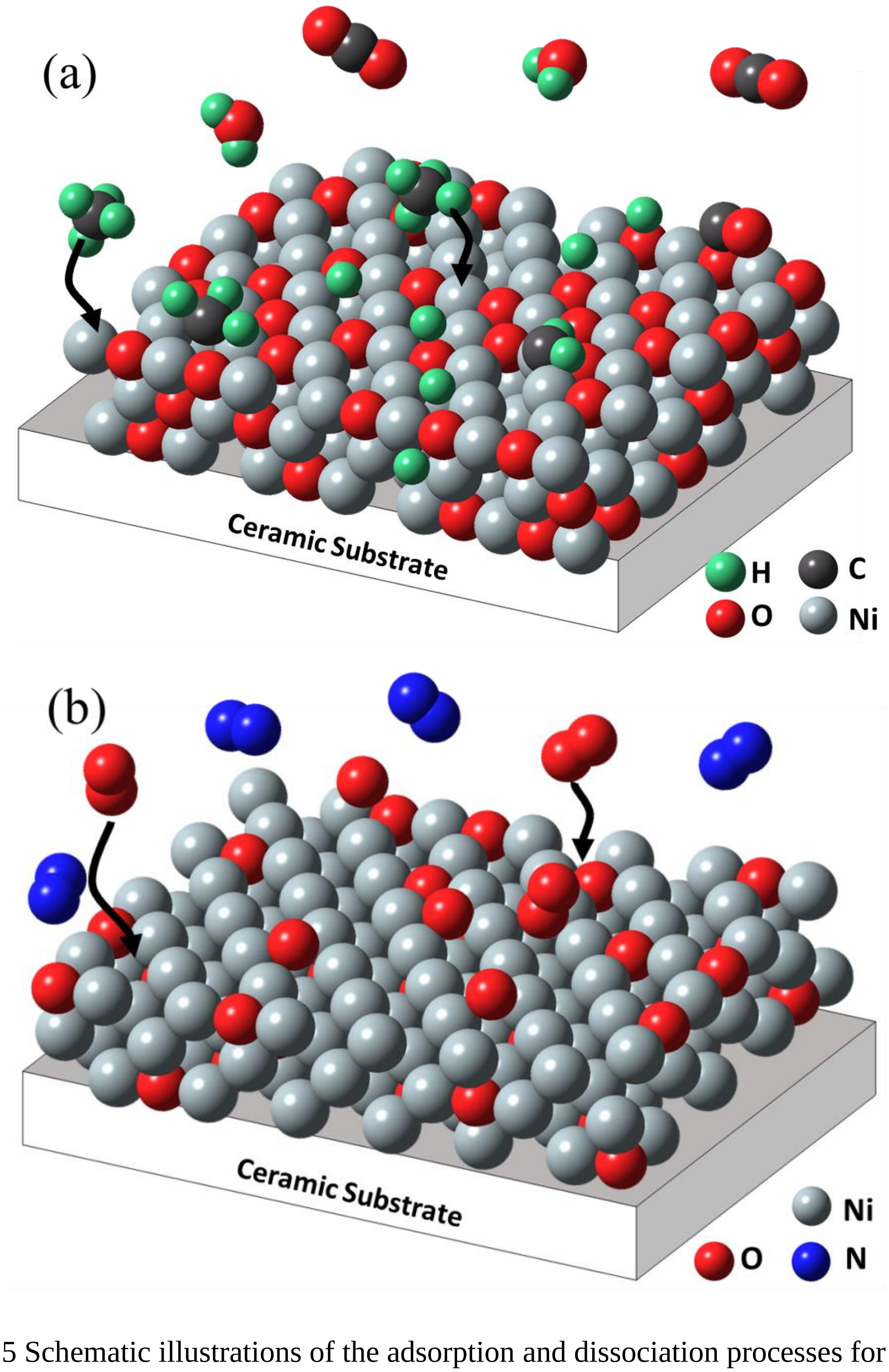

Figure 5 Schematic illustrations of the adsorption and dissociation processes for (a) NiO reduction with CH_4 (b) Ni oxidation with air

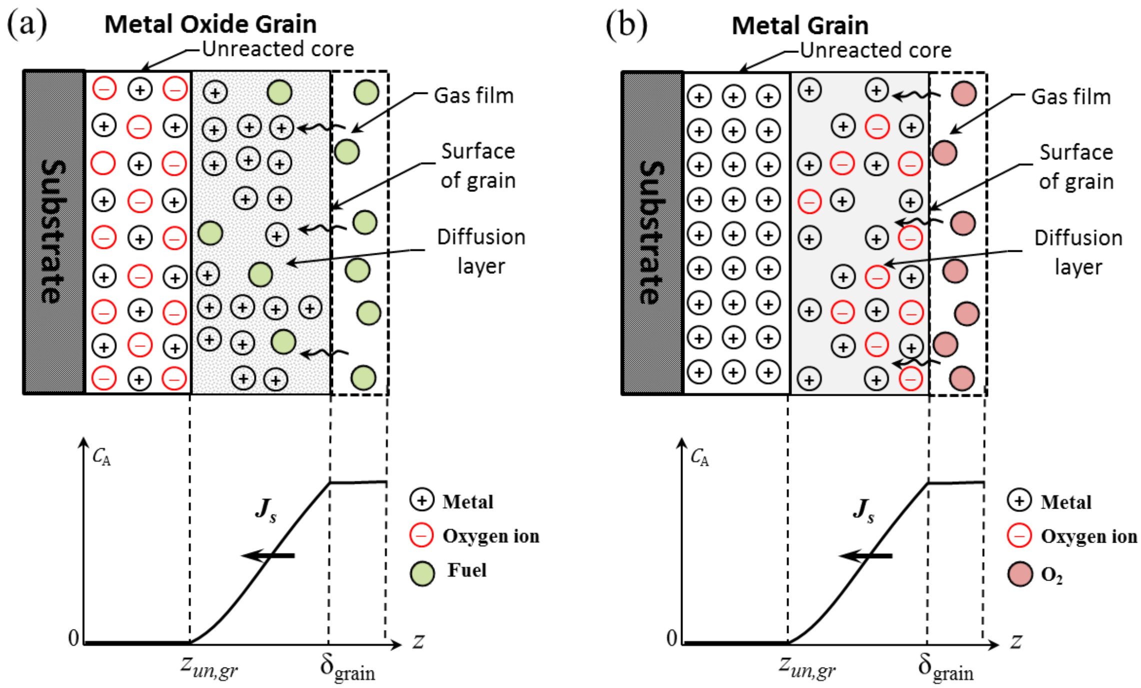

Figure 6 Schematic illustrations of the OC conversion under the control of the diffusion of the reactant through the grain for (a) reduction and (b) oxidation.

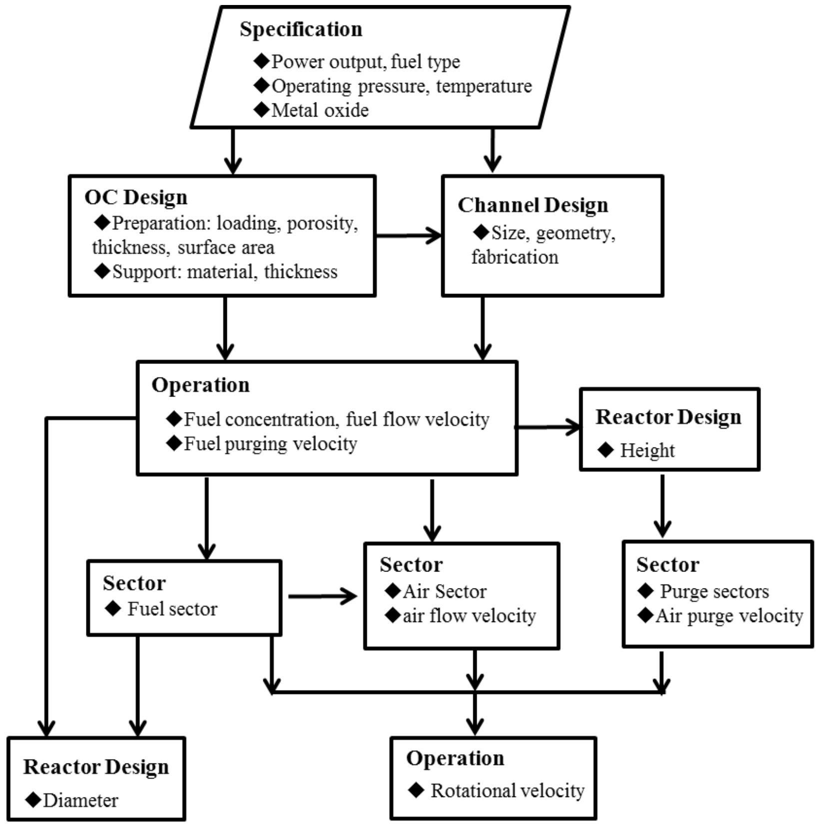

Figure 7 Design procedure of the rotary CLC reactor.

Table 1 Algebra expressions for the characteristic time of conversion under the control of each resistance

#	Resistance	Conversion equations	Characteristic time of conversion	Damköhler number
1	External diffusion to the OC surface	$X_B = t/\tau_{ex}$	$\tau_{ex} = \dfrac{\hat{\rho}_B \delta_{oc}}{\nu_r h_m C_A}$	$Da_{ex} = \dfrac{s_{oc}\tilde{\rho}_s k_r \delta_{oc}}{h_m}$
2	Internal diffusion through pores	$X_B^2 = t/\tau_{in}$	$\tau_{in} = \dfrac{\hat{\rho}_B \delta_{oc}^2}{2\nu_r C_A D_e}$	$Da_{in} = \dfrac{s_{oc}\tilde{\rho}_s k_r \delta_{oc}^2}{2D_e}$
3	Adsorption and dissociation	$X_B = t/\tau_{ad}$	$\tau_{ad} = \dfrac{\hat{\rho}_B}{\nu_r s_{oc}\tilde{\rho}_s k_{ad} C_A}$	$Da_{ad} = \dfrac{k_r}{k_{ad}}$
4	Diffusion in the product layer of a grain	$X_B^2 = t/\tau_{d,g}$	$\tau_{d,g} = \dfrac{\hat{\rho}_B \delta_{grain}}{2\nu_r s_{oc} C_A D_{e,g}}$	$Da_{d,g} = \dfrac{\tilde{\rho}_s k_r \delta_{grain}}{2D_{e,g}}$
5	Chemical reaction in the grain	$-\ln(1 - X_B) = t/\tau_r$	$\tau_r = \dfrac{\hat{\rho}_B}{\nu_r s_{oc}\tilde{\rho}_s k_r C_A}$	–

Table 2 Properties of the metal oxides used in CLC with CH_4 as fuel.

	CuO/Cu	NiO/Ni	Fe_2O_3/Fe_3O_4
Reduction	$CH_4+4CuO=CO_2+2H_2O+4Cu$	$CH_4+4NiO=CO_2+2H_2O+4Ni$	$CH_4+12Fe_2O_3=CO_2+2H_2O+8Fe_3O_4$
ΔH_0 [80]	-178.1 kJ/mol	156.5 kJ/mol	136.6 kJ/mol
Oxidation	$O_2+2Cu=2CuO$	$O_2+2Ni=2NiO$	$O_2+4Fe_3O_4=6Fe_2O_3$
ΔH_0 [80]	-312.1 kJ/mol	-479.4 kJ/mol	-469.4 kJ/mol
γ_{CH4} (800/1000/1200℃)	100%/100%/100%	100%/99%/98%	100%/100%/100%
R_O	0.20	0.21	0.03
melting point [36]	1446℃/1085℃	1955℃/1455℃	1565℃/1597℃
material cost	intermediate	high	low
carbon deposition	low	high	low

.

Table 3 Thermal conductivity of ceramic materials suitable for the rotary CLC reactor

		Conductivity ($W\ m^{-1}\ K^{-1}$)	Ref.
BN	Boron Nitride	200-600	[81]
BeO	Beryllium Oxide	50-200	[82]
AlN	Aluminum Nitride	50-200	[83]
SiC	Silicon Carbide	50-300	[84]
Al_2O_3	Aluminium Oxide	10-30	[82]
Si_3N_4	Silicon Nitride	10-30	[85]

Note: Typical values under the conditions of interest for rotary CLC.
The data varies with temperature, material structure, and preparation method.

Appendix A

The exergy or availability of a system measures the theoretical maximum work output during a thermal cyclic process. In a typical CLC setup, the oxidation reaction is highly exothermic ($\Delta H_{ox} < 0$) while the reduction reaction is endothermic ($\Delta H_{red} > 0$) or mildly exothermic ($\Delta H_{red} < 0$). Additionally, the two reactors may be operated under different temperatures, and hence it is theoretically possible to install a secondary Carnot engine between the two reactors that extracts additional work while reversibly transferring heat from the oxidation to the reduction reactor.

In panel a of Figure A1, we assume that the two reactors operate reversibly and isothermally and thus can be treated as heat reservoirs. Exhaust streams from the reactors are used to preheat the feed fuel and air streams in ideal heat exchangers. The heat exchangers are also assumed to be balanced so that the inlet streams leaving the exchanger are perfectly heated up to the respective reactor temperatures. The heat extracted/added to maintain an isothermal reaction is equal to the heat of that reaction. Hence, $-\Delta H_{ox} = Q_H$ and $-\Delta H_{red} = Q_C$. Therefore, $-\Delta H_r = -(\Delta H_{ox} + \Delta H_{red}) = Q_H + Q_C$. The temperatures of the air reactor and the fuel reactor are T_H, and T_C, respectively. Applying the first and second laws of thermodynamics to the control volume (inside the dashed box), the maximum work for cases where the reduction reaction is endothermic or exothermic is given by

$$-W_{\max,\mathrm{ex}} = |\Delta H_r|\left(1-\frac{T_0}{T_H}\right) - |\Delta H_{red}|T_0\left(\frac{1}{T_C}-\frac{1}{T_H}\right) \text{ (A1)}$$

$$-W_{\max,\mathrm{en}} = |\Delta H_r|\left(1-\frac{T_0}{T_H}\right) + |\Delta H_{red}|T_0\left(\frac{1}{T_C}-\frac{1}{T_H}\right) \text{ (A2)}$$

From Eq. (A1), it is obvious that the work output for the CLC system with exothermic reduction reaction is highest when $T_H = T_C$. In this case, both reactors supply the energy for the power generation, and hence a higher reduction temperature (T_C) provides heat with a higher quality.

For the case with endothermic reduction reaction, Eq. (A2) suggests that the system work output increases with the difference between the oxidation and the reduction reactor temperatures. This is because the two steps in CLC upgrade the low quality heat (at T_C) from the fuel reactor to the air reactor (at T_H) and more high-quality energy can be extracted in the air reactor at a higher temperature [1, 86, 87]. Therefore, theoretically, extra work output can be produced via the secondary engine as the heat is transferred from the air reactor (hot reservoir) to the fuel reactor (cold reservoir) to maintain the overall energy balance (see panel a of Figure A1).

However in a practical CLC system, it is less likely to install an engine between the two reactors to exchange heat while extracting work because the transferred energy is mainly in the form of the internal energy of the solids and it is transferred via the physical transport of the solids between the two reactors. Thus, in the absence of a secondary engine, the direct heat transfer results in exergy destruction proportional to the temperature difference. The entropy generation can be estimated as completely due to the heat transfer between the reactors and is given by

$$\dot{S}_{gen} = \Delta H_{red}\left(\frac{1}{T_C} - \frac{1}{T_H}\right) \text{ (A3)}$$

Thus, the maximum work output in this case (panel b of Figure A1) is

$$-W^{*}_{\mathrm{max,en}} = \left|\Delta H_r\right|\left(1 - \frac{T_0}{T_H}\right) \text{ (A4)}$$

Therefore, in this case, the maximum work output is independent on the selection of the temperature difference, and the thermodynamic advantage of operating the fuel reactor at a lower temperature disappears owing to the irreversibility associated with the heat transfer. From a practical point of view, it is preferred to operate the fuel reactor at the same temperature to reach a high reduction rate in the fuel reactor, and to minimize the thermal stresses caused by the temperature variations during the transport of the solids.

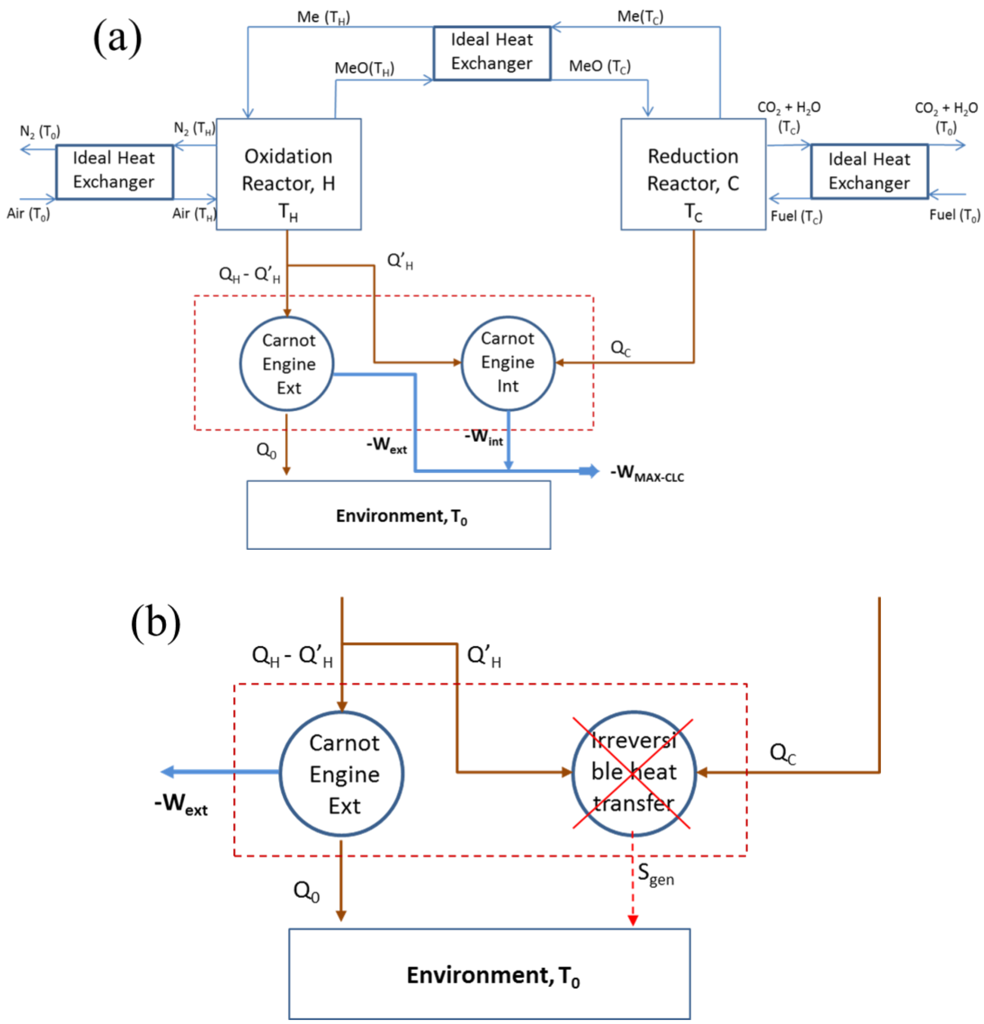

Figure A1 Schematic of (a) an ideal CLC reactor system (b) the entropy generation in practical CLC systems

Appendix B

The adsoprtion, and the chemical reaction processes can be described by Eley-Rideal reaction mechanism (Eq. (16) and (17)). If we assume that the adsorbed surface species, *AS*, and *S* are in quasi-steady states, therefore,

$$\theta_{AS} = \frac{k_1 C_A \theta_S}{k_{-1} + k_2 \phi_B} \quad \text{(B1)}$$

where k_1 and k_{-1} are the forward and reverse rate coefficients of reaction (16), and k_2 is the forward reaction rate of reaction (17). θ_S, and θ_{AS} are the coverage ratios of the available active sites, and the sites occupied by *AS*. The summation of θ_S and θ_{AS} equals unity. Thus,

$$\theta_S = \frac{k_{-1} + k_2 \phi_B}{k_{-1} + k_2 \phi_B + k_1 C_A} \quad \text{(B2)}$$

Thus, the overal reaction rate is:

$$-\frac{1}{v_r}\frac{dN_B}{dt} = \frac{N_s k_1 k_2 C_A \phi_B}{k_{-1} + k_2 \phi_B + k_1 C_A} \quad \text{(B3)}$$

By assuming the relative importance of the adsorption and the chemical reaction steps, we can simplify Eq. (B3) into:

$$-\frac{1}{v_r}\frac{dN_B}{dt} = k_1 N_s C_A \text{, adsorption controls (B4)}$$

$$-\frac{1}{v_r}\frac{dN_B}{dt} = \frac{N_s K_1 k_2 C_A \phi_B}{1 + K_1 C_A} \text{, chemical reaction controls (B5)}$$

where K_1 is the equilibrium constant of reaction (16). If $K_1 C_A << 1$, Eq. (B5) becomes identical to Eq. (5). In this case, the reaction rate rises with the increase of the reactant concentration, and the conversion is mainly controlled by the amount of avaiable reactant in the bulk phase. On the other hand, if the reaction proceeds with a high concentration of the reactant, i.e., $K_1C_A >> 1$, thus Eq. (B5) becomes:

$$-\frac{1}{v_r}\frac{dN_B}{dt} = N_s k_2 \phi_B \quad \text{(B6)}$$

In this case, the active sites on the grain lattice are saturated by the reactant, and a further increase in the reactant concentration has little effect on the reaction rate. Here the reaction is mainly controlled by the available sites (θ_S) on the surface. In addition, the product molecules in the reduction reaction, e.g., H_2O, CO_2, may adsorb onto the grain, block the active sites on the lattice surface, and hence further reduce θ_S. These effects may prevail at elevated pressures.